Measurements on isovector giant resonances in pion charge exchange

A. Erell, J. Alster, J. Lichtenstadt, and M. A. Moinester
School of Physics and Astronomy, Raymond and Beverly Sackler Faculty of Exact Sciences, Tel-Aviv University, Tel-Aviv 69978, Israel

J. D. Bowman, M. D. Cooper, F. Irom, H. S. Matis,* E. Piasetzky,† and U. Sennhauser‡
Los Alamos National Laboratory, Los Alamos, New Mexico 87545
(Received 24 April 1986)

We measured the energies, widths, and cross sections of the isovector monopole and dipole resonances in various nuclei between ^{40}Ca and ^{208}Pb with the reactions $(\pi^{\pm},\pi^{0})$. Both resonances exhaust approximately the same substantial fraction of the cross section calculated in a random-phase-approximation—distorted-wave-impulse-approximation model. The excitation energies and widths of the monopole and dipole are in good agreement with random-phase-approximation calculations and for the dipole they are also in agreement with other data. No isovector quadrupole resonance was observed, and the upper limits for the cross sections for the light elements are well below the sum rule strength for the isovector monopole and giant dipole resonance.

I. INTRODUCTION

Giant resonances are collective nuclear excitations in which many protons and neutrons move in a coherent manner. Thus, their study is fundamental to the understanding of nuclear structure and the nucleon-nucleon force in nuclei. Electric isoscalar ($\Delta T=0$) modes are characterized by oscillations of the nucleus as a whole, in which protons and neutrons move in phase. In the electric isovector ($\Delta T=1$) modes the protons oscillate in opposite phase to that of the neutrons. The magnetic modes are characterized by oscillations that differentiate spin ($\Delta S=1$). The different multipoles are characterized by the spatial symmetry of the oscillations. For example, a monopole mode is a spherically symmetric oscillation and a dipole vibration is axially symmetric. The giant resonances can also be described, microscopically, as coherent sums of one-particle—one-hole excitations between major oscillator shells. For the electric modes, the angular momentum of the particle-hole pair determines the multipolarity of the excitation. The well-known giant dipole resonance involves excitations of one major shell ($1\hbar\omega$) and has angular momentum and parity 1^{-}. The isovector monopole and isovector quadrupole resonances are $2\hbar\omega$ excitations and have angular momentum and parities of 0^{+} and 2^{+}, respectively.

Isoscalar resonances are formed by $T=0$ and isovector modes by $T=1$ particle-hole states. The residual particle-hole interaction gives rise to the formation of a collective state which is strongly shifted in energy with respect to the unperturbed particle-hole energy. The attractive isoscalar residual interaction shifts isoscalar modes to lower energies and the repulsive isovector residual interaction shifts isovector modes to higher energies. For isoscalar resonances, transitions connect states of the same isospin in the same nucleus. For isovector resonances transitions are allowed for which $T\rightarrow T-1$, T, $T+1$, excluding $T=0\rightarrow T=0$. These selection rules govern the isospin transitions for isovector resonances as shown in Fig. 1. The distribution of transition strength to different isospin components in the Z or $Z\mp1$ nuclei is related to isospin coupling coefficients[1] and favors transitions to the lowest isospin state. Another property of the strength distribution is that the transition to the $T+1$ component in the $Z-1$ nucleus is weaker relative to both the T component in the Z nucleus and the $T-1$ in the $Z+1$ nucleus due to Pauli blocking in the transformation of a proton into a neutron. This blocking increases with the isospin of the target nucleus and is larger for $1\hbar\omega$ than for $2\hbar\omega$ transitions.

Giant resonances should have the following qualitative characteristics: (a) a resonance should exhaust a large fraction of the energy-weighted sum rule (EWSR) or the non-energy-weighted sum rule in an energy region which is narrow relative to its excitation energy; (b) the resonance should exist in a wide range of nuclei and its energy and width should vary smoothly with mass number, A. The isovector giant, dipole resonance (GDR) was first observed in photon absorption experiments.[2] It is excited strongly in photonuclear reactions that selectively excite $L=1$, $T=1$ states. Isoscalar $L=0$, 2, and 3 resonances were observed later[3] and studied in detail in electron and hadron scattering. Alpha scattering proved to be the most useful reaction for studying the isoscalar monopole and quadrupole resonances since it excites only $T=0$ states. In contrast to isoscalar modes, isovector electric resonances other than the GDR are not yet well established. Specifically, the properties of an isovector monopole excitation (IVM) were calculated in both macroscopic[4] and microscopic[5,6] theories, but this excitation was not observed until the present experiment.[7,8] There are also detailed predictions of the properties of an isovector quadrupole resonance (IVQ) and evidence has been given for its existence in electron scattering[9] and (n,γ) reactions.[10,11] However, it has not yet been shown to satisfy the above criteria.[12]

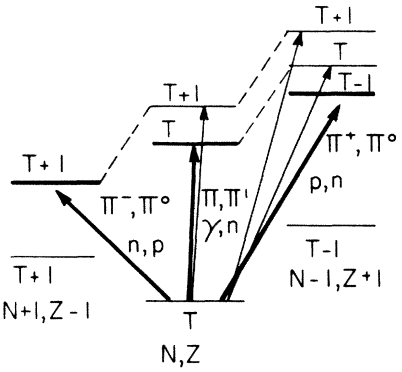

FIG. 1. Allowed isospin transitions for isovector resonances. The dashed lines connect states of the same isospin multiplet. In neutron-rich nuclei the transitions to the lowest isospin components (thick lines) are favored. In $N=Z$ nuclei ($T=0$) transitions are allowed only to the $T+1$ multiplet. Several reactions that may be used to excite these isospin components are listed.

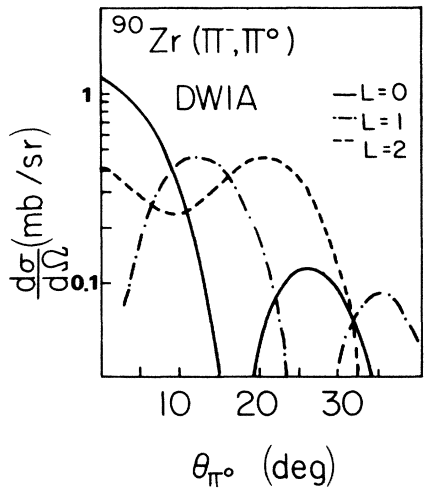

FIG. 2. DWIA calculations of pion charge-exchange angular distributions at 165 MeV for $L=0$, 1, and 2 giant resonances. The shapes resemble the diffractive Bessel function relations. Note that the $L=0$ and 2 angular distributions are clearly distinguishable.

The study of new isovector resonances will yield information on the isospin dependence of the N-N interaction in nuclei, which contributes to the symmetry energy in nuclei. A special interest in the IVM stems from the fact that it plays a major role in Coulomb effects, such as isospin mixing in nuclear ground states, Coulomb displacement energies, and widths of analog states.[13] Several arguments led us to believe that the pion charge-exchange reaction, particularly (π^-,π^0), would be highly selective for the excitation of the IVM. Thus in the present work we carried out a systematic search for the IVM with the $(\pi^\pm,\pi^0)$ reactions in a wide range of nuclei. Additional objectives were to study alternate isospin components of the well-known GDR, and to search for the IVQ. Our experimental tools were the LAMPF π^0 spectrometer and the intense monochromatic positive and negative pion beams available at LAMPF.

The advantageous features of pion charge-exchange reactions for studying isovector resonances, particularly the IVM, can be understood as follows.

(I) Inelastic scattering with a probe of nonzero isospin populates states having isospin greater than or equal to the target ground state isospin T. (The maximum value of the final state isospin is determined by the triangle inequality.) In inelastic scattering isovector states such as the GDR or IVM will be superimposed on a large background of isoscalar states having isospin T. The charge exchange (π^-,π^0) reaction populates states having isospin $T+1$ or greater. The large background of isoscalar states has no analogs in the (π^-,π^0) daughter and hence is absent.

(II) Near the 3,3 resonance the pion charge-exchange reaction takes place mostly at the surface of the nucleus and the pronounced maxima of the angular distributions allow a direct determination of the angular momentum transfer.[14,15] This is demonstrated in Fig. 2, where distorted-wave-impulse-approximation (DWIA) calculations[6] of the angular distributions for $L=0$, 1, and 2 multipoles are plotted. We note that the $L=0$ and 2 multipoles are easily distinguished by the ratios of the cross sections in the first maximum to the cross sections in the second maximum, which is approximately 10 for $L=0$ and 0.7 for $L=2$. This is in contrast to nucleon charge exchange at energies up to several hundred MeV, in which the $L=0$ and 2 shapes are not very different.[16]

(III) In pion-nucleus interactions the excitation of background states due to spin-flip transitions is suppressed at forward angles because the pion is spinless and interacts with the spin of the nucleons only through the pion orbital angular momentum. This is in contrast to nucleon charge exchange at energies of several hundred MeV, which predominantly excite spin-flip transitions.

(IV) The strong pion-optical absorption provides the strongest overlap of the pion wave function with the exterior part of the transition densities. This is important for the excitation of the IVM since the integral over the entire nuclear volume of the monopole transition density vanishes. The cross section at forward angles would be reduced for probes that sample the entire nuclear volume, such as electrons.

(V) The (π^-,π^0) reaction is especially suitable for the search for the IVM because the IVM in the target nucleus is expected at high excitation energies ($170A^{-1/3}$ MeV; see Ref. 4). It lies in a region of very high density of states with a large escape width. On the other hand, the $T+1$ component, excited by the (π^-,π^0) reaction, is lowered by the Coulomb displacement energy (see Fig. 1) and is therefore expected to be relatively narrow. The opposite is true for the IVM excited by (π^+,π^0). In addition, in the π^- reaction all the transition strength is concentrated in one isospin component, whereas the splitting in the π^+ reaction increases the observed width. This effect, however, becomes smaller as the isospin of the target nucleus increases because the transitions to the lowest iso-

spin component become increasingly dominant.

(VI) Another advantage of the (π^-,π^0) over the (π^+,π^0) reaction is related to the fact that the difference in the IVM and GDR excitation energies is of the order of the experimental π^0 energy resolution (6 MeV), and the peaks of the two resonances therefore partially overlap. In the π^- reaction on the heavy-element targets the $1\hbar\omega$ GDR is suppressed by Pauli blocking to a greater extent than the $2\hbar\omega$ IVM and therefore interferes less with the IVM.

(VII) Finally, there is an experimental aspect that makes the $(\pi^\pm,\pi^0)$ reaction favorable for detecting the IVM. Whereas many experiments cannot easily be carried out at forward angles, where the IVM cross section peaks, the π^0 spectrometer used in the present work is especially suitable for zero-degree measurement.

The selection rules for $(\pi^\pm,\pi^0)$ reactions offer advantages for studying the isospin structure of isovector resonances. In heavy nuclei, where (π^+,π^0) excites mainly the $T-1$ state, the comparison of the states excited by $(\pi^\pm,\pi^0)$ should yield the $T+1, T-1$ isospin splitting when the Coulomb energies are taken into account. For the GDR, a comparison with the T component excited by (γ,n) reactions will yield the $T+1, T$ and $T, T-1$ splittings as well. The fact that the spin-flip transitions are suppressed for pion scattering at small angles means that the states excited by the pion charge-exchange reactions are the analog isospin components of the photonuclear GDR, which is predominantly a non-spin-flip excitation.

In this paper we present the results of a systematic study of the IVM, GDR, and IVQ with $(\pi^\pm,\pi^0)$ reactions. Some of the results have been published in Refs. 7, 8, and 17; here we give a complete account of the experiment. We emphasize that the results for all the resonances are extracted using the same analysis procedure. Thus, the extent to which there is agreement between the extracted GDR properties and other data is a measure of the validity of the data analysis and therefore of the results for the IVM and IVQ. The (π^+,π^0) cross sections for the isobaric analog states (IAS's) have also been measured in the present work. The results are not discussed since they have already been published.[18] The experimental details are described in Sec. II and the data analysis is given in Sec. III. There we also discuss the nonresonant background whose determination constituted the major effort of the analysis. In Sec. IV we present the results for the IVM and GDR and report upper limits for the IVQ. In Sec. V we give a short description of the RPA-DWIA calculations (RPA denotes random-phase approximation) by Auerbach and Klein[6] and compare them to the data. We also compare the GDR results to existing data. The results are discussed in Sec. VI with conclusions in Sec. VII.

II. EXPERIMENTAL PROCEDURE

The data were taken at the LEP channel at LAMPF. Targets of ^{40}Ca, ^{60}Ni, ^{90}Zr, ^{120}Sn, ^{140}Ce, and ^{208}Pb were bombarded with 165 MeV π^- and π^+. The beam-momentum resolution was better than 1.3% and the rates were typically 10^7 pion/s. The flux was determined and frequently monitored by an activation method.[19] The energy and direction of the outgoing π^0 were measured with the LAMPF π^0 spectrometer by measurement of the angle and energy of the two gamma rays from the π^0 decay. A detailed description of the spectrometer is given in Refs. 20 and 21. The front converters of the spectrometer were at a distance of 1 m from the target and the opening angle between the two gamma detectors was 62.3°. The bulk of the data was taken in late 1982 with the spectrometer set at scattering angles of 5° and 25°, and some data were taken a year earlier under slightly different conditions. Enriched targets were used of thicknesses ranging from 1.8 to 4 g/cm^2. The total number of pions per spectrometer setting ranged from 1.2×10^{11} for the lighter nuclei to 3.8×10^{12} for ^{208}Pb.

At each fixed position the spectrometer covered an angular range of approximately 20°. The angular range was divided into four angle bins; the acceptance as a function of angle inside the individual bins was calculated with a Monte Carlo simulation.[21] The average angles and rms bin widths for the various angular bins are given in Table I. The angular resolution of the spectrometer was approximately 2.5°. However, with the above binning of the angular acceptance, the resolution was determined by the bin widths (given in Table I), and was approximately 5°. As the target enrichments were close to 100%, we assumed the abundances were 100% since all isotopes should have about the same cross sections.

The reaction $\pi^-p\rightarrow\pi^0n$ on a CH_2 target was used for calibrations of energy and solid angle. The energy calibration and resolution were determined from the position and width of the π^0 peak in the most forward bin, where the proton recoil is negligible. The spectrometer energy resolution was compromised to 6 MeV in order to achieve good statistics. The effective solid angle of the spectrometer is a function of π^0 energy and angle. It was determined by comparing the $\pi^-p\rightarrow\pi^0n$ yields to the calculated cross sections, using phase shifts of Rowe *et al.*[22] The CH_2 data were taken at π^- energies of 100, 120, 130, 140, 150, and 165 MeV at the 5° and 25° spectrometer positions. The carbon contribution was subtracted using measurements with a graphite target. Figure 3 shows the effective solid angle for the most forward angular bin at the various energies. It reaches a maximum at 130 MeV, corresponding to the opening angle between the gamma detectors. For each angular bin the spectrometer acceptance as a function of energy was obtained by a smooth interpolation (solid line). The measured solid angles were used to correct the π^0 energy spectra channel by channel. In the final determination of the cross sections, the absorption of gammas in the targets was taken into account. The correction factors are given in Table I.

The error bars in Fig. 3 do not include the uncertainty in the $\pi^-p\rightarrow\pi^0n$ cross sections, which are approximately 5% in the energy region of the giant resonances. The ratios of the effective solid angles to those calculated by the Monte Carlo simulation determine the counting efficiency and should be, in principle, angle independent. Their actual values fluctuated by 4% from angle to angle, which is slightly larger than the statistical error in the π^-p measurements. Thus, a 4% relative error was assigned to the angular variation of the effective solid angle.

TABLE I. Average values and standard deviations of the angular acceptance for the various angular bins.

Spect. position	$\langle\theta\rangle$ (deg)	σ_θ	T_{π^0} FWHM (MeV)	Spect. position	$\langle\theta\rangle$ (deg)	σ_θ	T_{π^0} FWHM (MeV)
5°	4.2	2.0	5.9	0°	4.5	1.1	4.5
	6.8	2.1	5.9		6.9	0.9	4.5
	10.5	1.8	6.4		11.0	2.0	5.2
	14.9	2.0	6.7		15.1	2.9	5.5
	17.4	2.3	6.3				
25°	22.8	1.9	7.1	20°	22.0	1.7	6.0
	27.7	1.9	7.1		28.5	2.5	6.0
	33.2	2.1	8.0				

Background due to random coincidences between the gamma detectors, which was determined from the timing spectrum, and non-target-related background, were subtracted from the spectra channel by channel. Each one of these corrections was of the order of 5–10%. Hydrogen contaminations in the ^{40}Ca, ^{60}Ni(π^-,π^0) data were subtracted using the CH_2 data. The amount of contamination was calculated from the data at the most forward angle, where the $\pi^-p\rightarrow\pi^0n$ cross section is largest and the $\pi^-p\rightarrow\pi^0n$ peak occurs at an energy that is higher than that of events from the target. Figure 4(a) shows a ^{40}Ca(π^-,π^0) spectrum, uncorrected for the acceptance of the spectrometer, (1) before and (2) after subtraction of the three background contributions. Figure 4(b) shows the above spectrum (2), corrected for the acceptance of the spectrometer.

III. DATA ANALYSIS

A. Background determination and analysis procedure

Figure 5 shows plots of the double-differential cross section for the (π^-,π^0) reactions versus the kinetic energy of the π^0's at four of the measured angles. A complete set of data can be found in Erell *et al.*[7] Figure 6 shows the plots for (π^+,π^0). An examination of the data shows IVM, GDR, and IAS (only in the π^+ data) excitations superimposed on an approximately isotropic nonresonant background. The IAS is clearly seen in the forward-angle (π^+,π^0) spectra. In most of the central-angle spectra the GDR is seen as a peak at approximately the energies known from earlier work.

In order to identify the broader IVM, the angular variation as well as the energy dependence of the cross sections had to be considered. In Fig. 7(a) we demonstrate the presence of a forward-peaked signal in a wide range of nuclei for the (π^-,π^0) reaction. We plot the ratio of the cross section, integrated over the expected IVM region, to the cross section integrated over the whole spectrum, versus q^2. Here, q is defined as the momentum transfer in a quasifree reaction, $q\simeq 2k_\pi\sin(\theta/2)$. There is a q^2 region in which the ratio is approximately linear, while at small q^2 there is an excess cross section above the straight line extrapolated to $q^2=0$. The observed breaking points

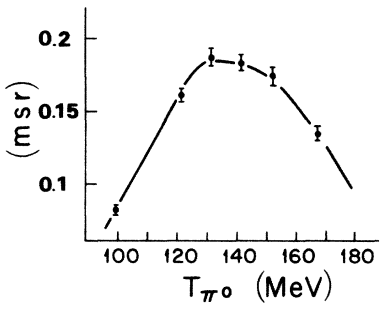

FIG. 3. The effective solid angle of the spectrometer for the 4° angular bin, as measured with the $\pi^-p\rightarrow\pi^0n$ reaction at various π^- energies. The acceptance angle of the spectrometer was smoothly interpolated as a function of energy between the measured points (solid line) and was used to correct the energy spectra channel by channel. The effect of the acceptance correction is demonstrated in Fig. 4.

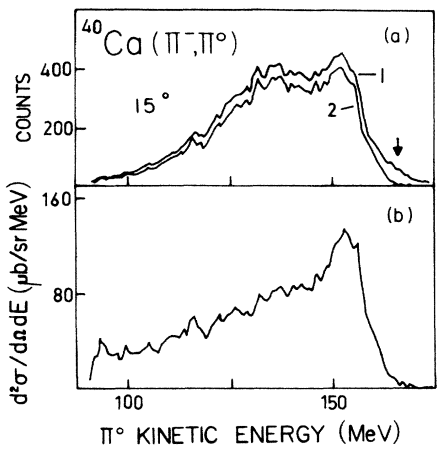

FIG. 4. ^{40}Ca(π^-,π^0) spectra. (a) Uncorrected for the spectrometer acceptance, (1) without and (2) with subtraction of the nonphysical background. The arrow points to the position of the small excess cross section due to hydrogen contamination. (b) The above background-subtracted spectrum (2) corrected for the acceptance of the spectrometer.

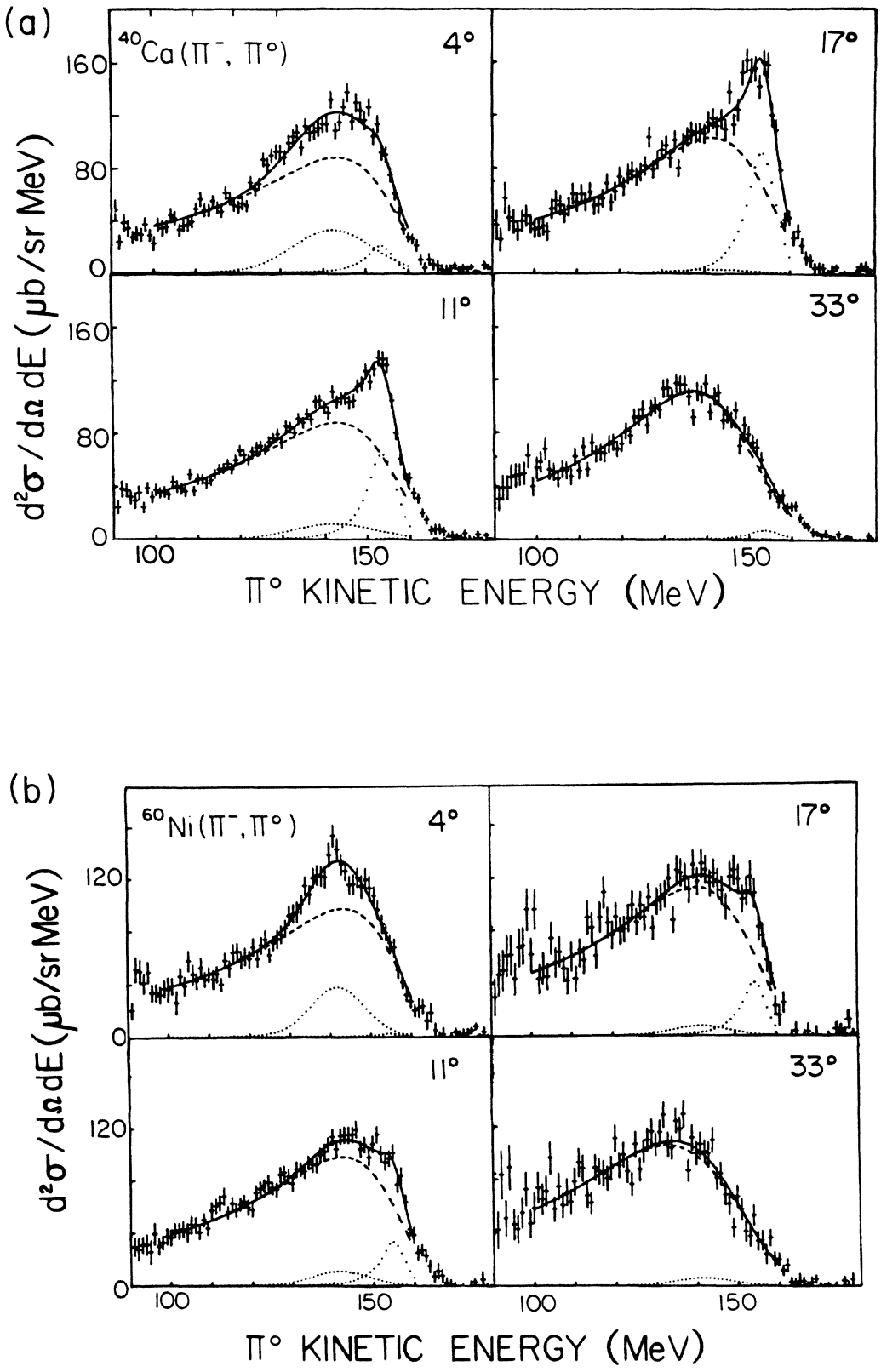

FIG. 5. Double-differential cross sections for the (π^-,π^0) reaction on (a) ^{40}Ca, (b) ^{60}Ni, (c) ^{90}Zr, (d) ^{120}Sn, (e) ^{140}Ce, and (f) ^{208}Pb. The dashed lines show the fitted background component. The dotted lines show the fits to the IVM (left-hand peak) and GDR (right-hand peak) and the solid line represents the fit to the sum.

appear near the angles of the first minimum of the expected IVM angular distributions, as indicated by arrows. Figure 7(b), for the corresponding ratio at an excitation energy above the IVM in ^{60}Ni, shows no indication of a forward-peaked feature. This qualitative analysis suggests that the cross section is composed of a slowly varying background component, approximately linear in q^2, and a forward-peaked feature around the expected IVM energy. In Sec. IV B, we discuss the linear q^2 dependence of the background. The reason for plotting ratios rather than absolute cross sections is to eliminate relative normalization errors between the 5° and 25° spectrometer settings.

For ^{40}Ca the presence of the IVM cannot be clearly demonstrated in an analysis such as is shown in Fig. 7.

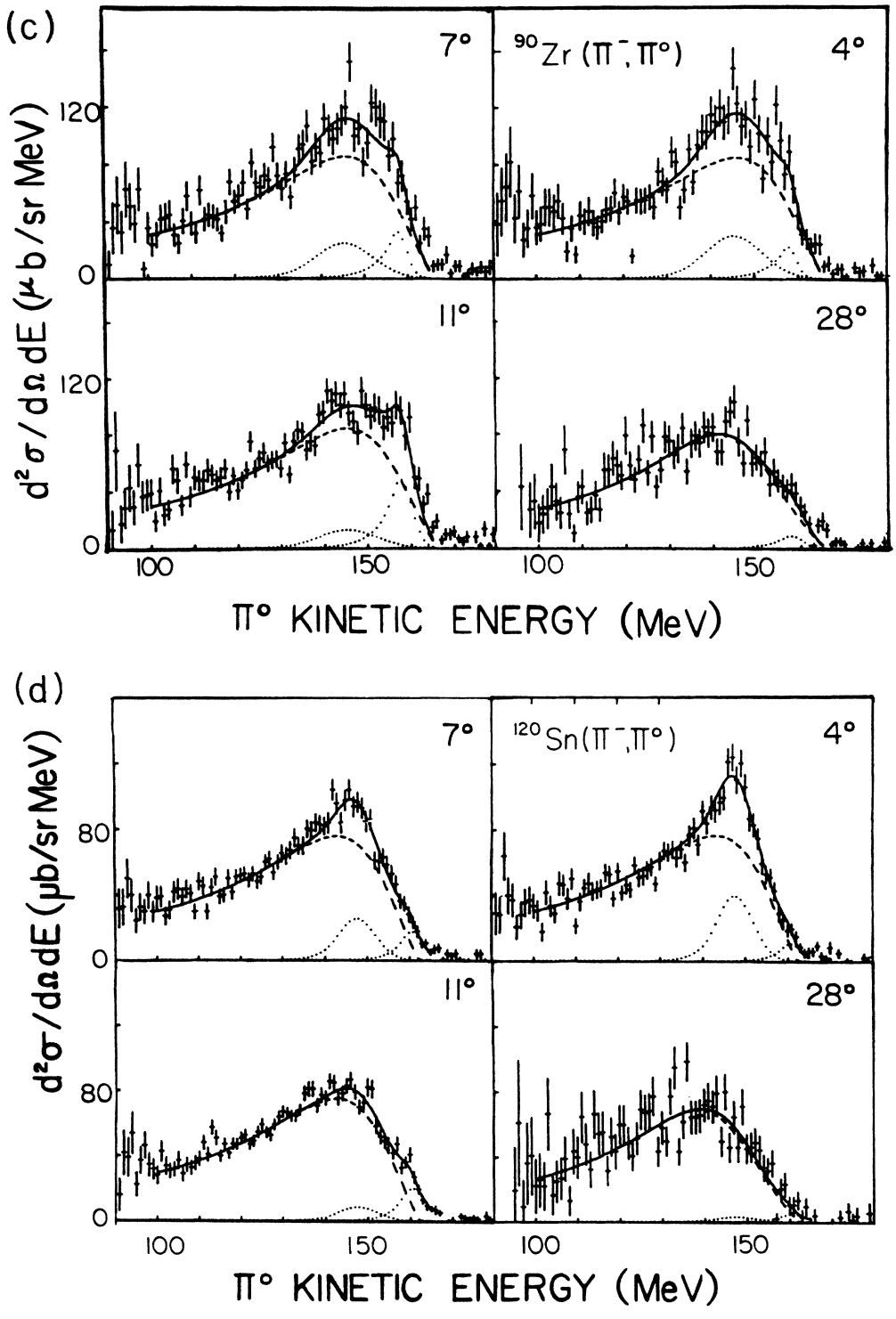

FIG. 5. (*Continued*).

The reason is that the first minimum of the IVM angular distribution occurs between the fifth and sixth angular bins, and the background cannot be extrapolated unambiguously using the data only in the three largest q^2 bins. For (π^+,π^0) the larger width of the IVM and the strong overlapping GDR make the signal-to-background ratios less favorable than for (π^-,π^0). Figure 7 is as relevant for the IVQ as for the IVM since their excitation energies calculated in the RPA differ by only a few MeV. There is no indication of any increase in the cross section near the expected peak (indicated by the dotted arrows) of IVQ angular distributions.

This qualitative analysis indicates that in order to extract quantitatively an IVM signal from the data and to

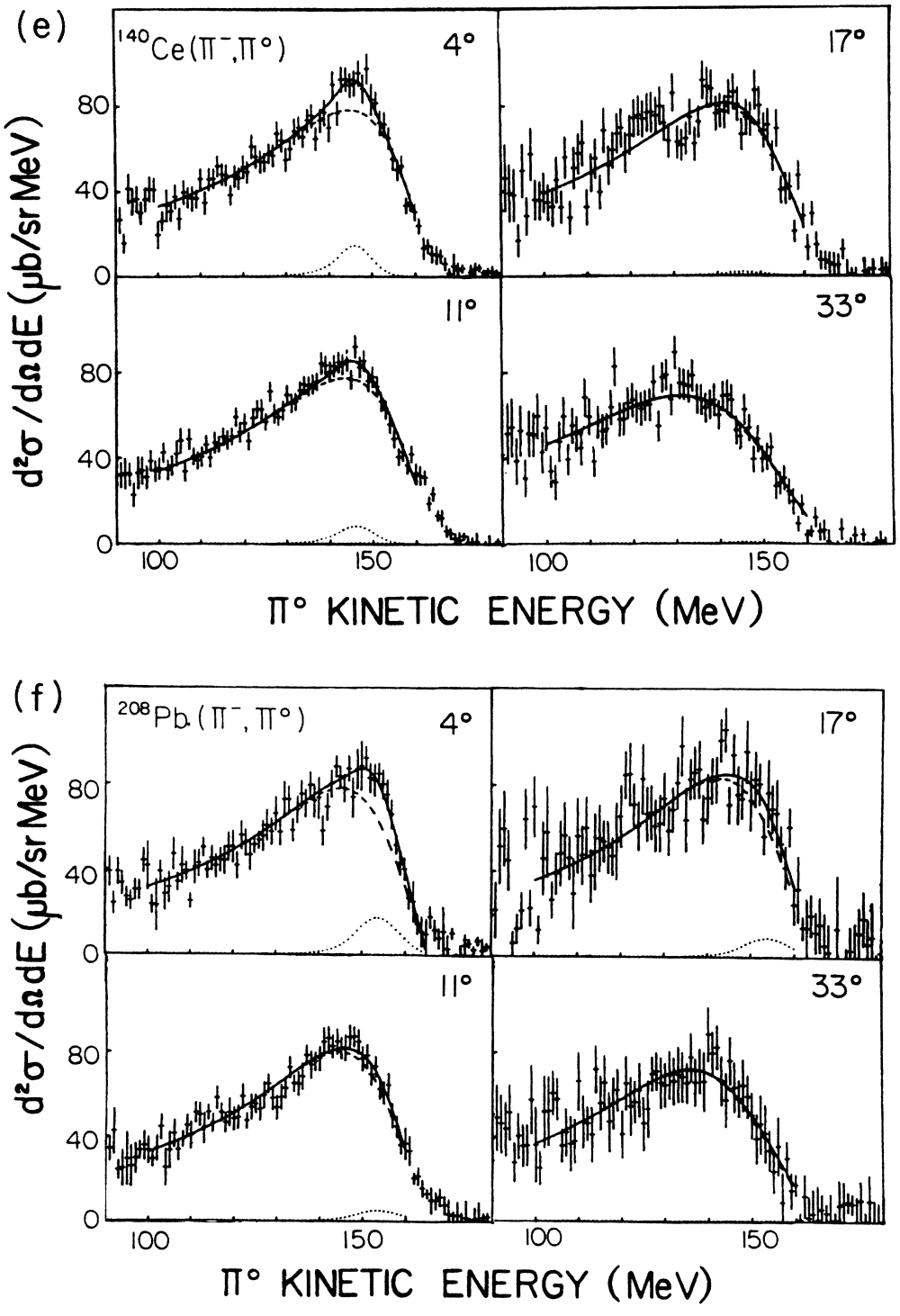

FIG. 5. (*Continued*).

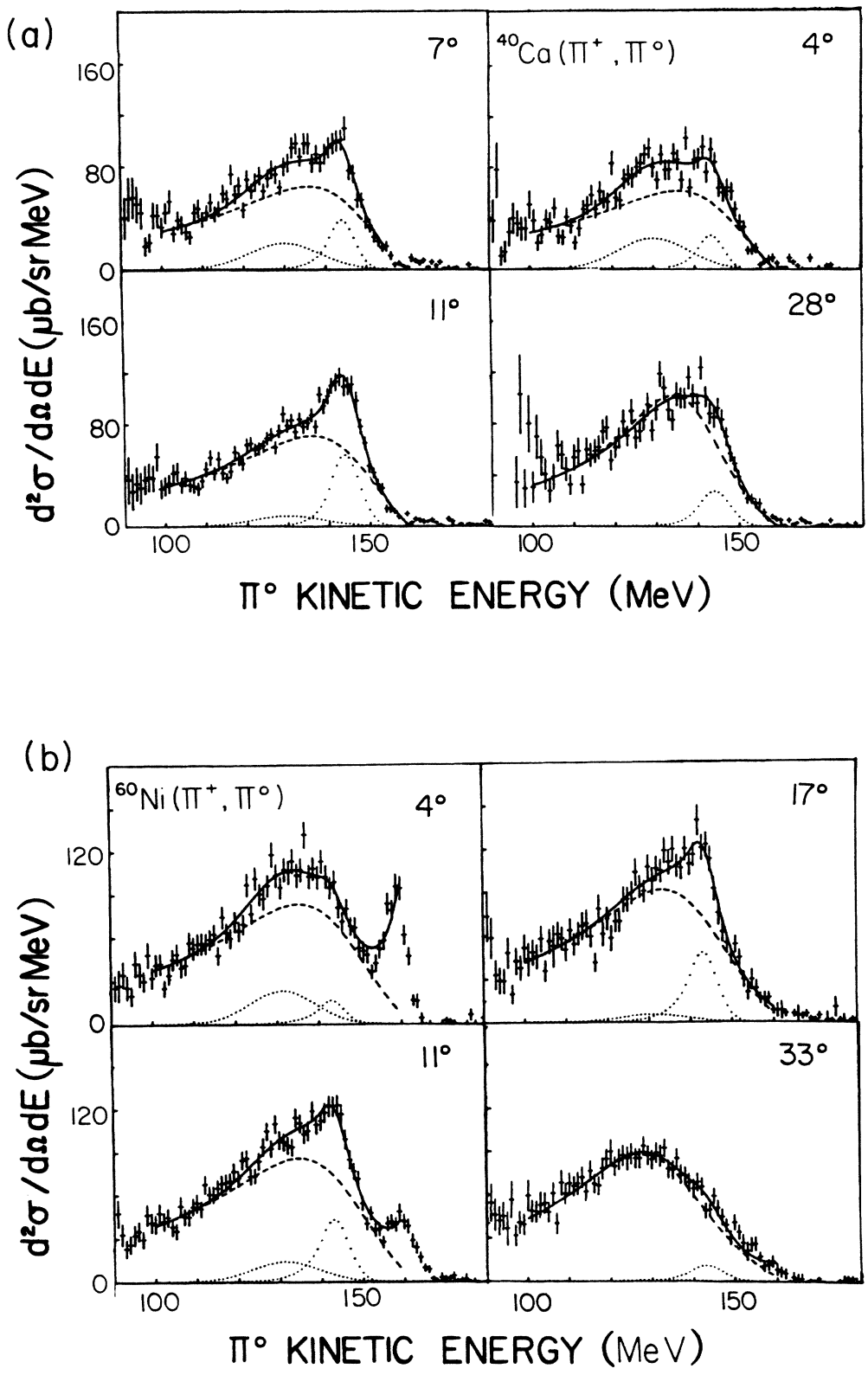

FIG. 6. Double-differential cross sections for the (π^+,π^0) reactions on (a) ^{40}Ca, (b) ^{60}Ni, (c) ^{90}Zr, (d) ^{120}Sn, (e) ^{140}Ce, and (f) ^{208}Pb. The dashed lines show the fitted background component. The dotted lines show the fits to the IVM (left-hand peak) and GDR (right-hand peak) and the solid line represents the fit to the sum. The sharp peak in the forward angles spectra (excluding ^{40}Ca) is the IAS.

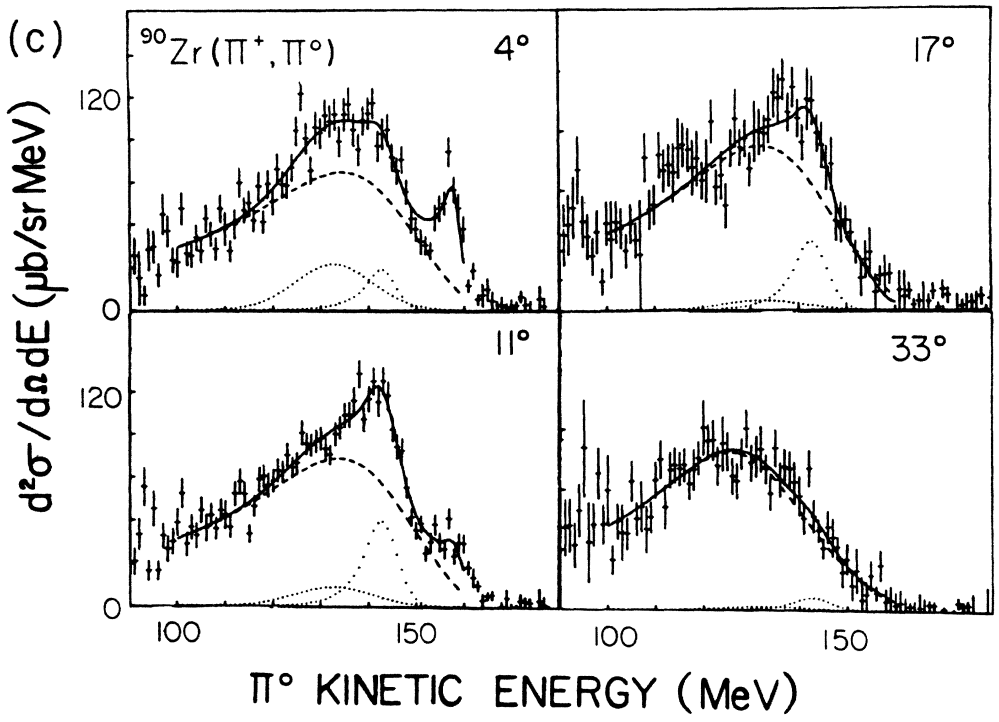

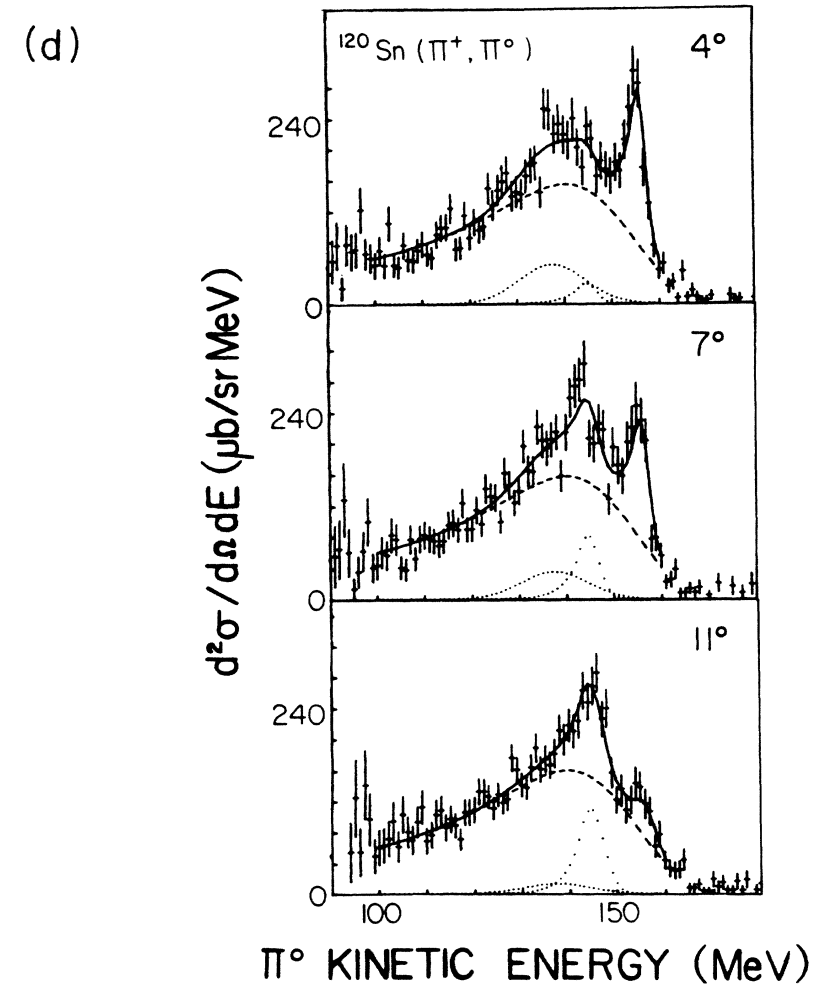

FIG. 6. (*Continued*).

establish uncertainties, a systematic procedure had to be developed for the description of the nonresonant background. Thus, the data were considered in the two-dimensional space of q^2 and energy loss ν. The giant resonances contribute to the cross section only in limited regions of this space. The double-differential cross section was fitted to a sum of IVM, GDR, and nonresonant components. At a later stage an IVQ component was also considered (see Sec. IV B). A semiphenomenological background function was chosen, which fitted the data well in those regions of large q^2 and excitation energies, where the IVM and GDR contributions are small. Such regions appear especially in the (π^-,π^0) data in the heavy elements, where Pauli blocking strongly suppresses the GDR cross section and the first minimum of the IVM angular distribution occurs at small q^2. The function has a

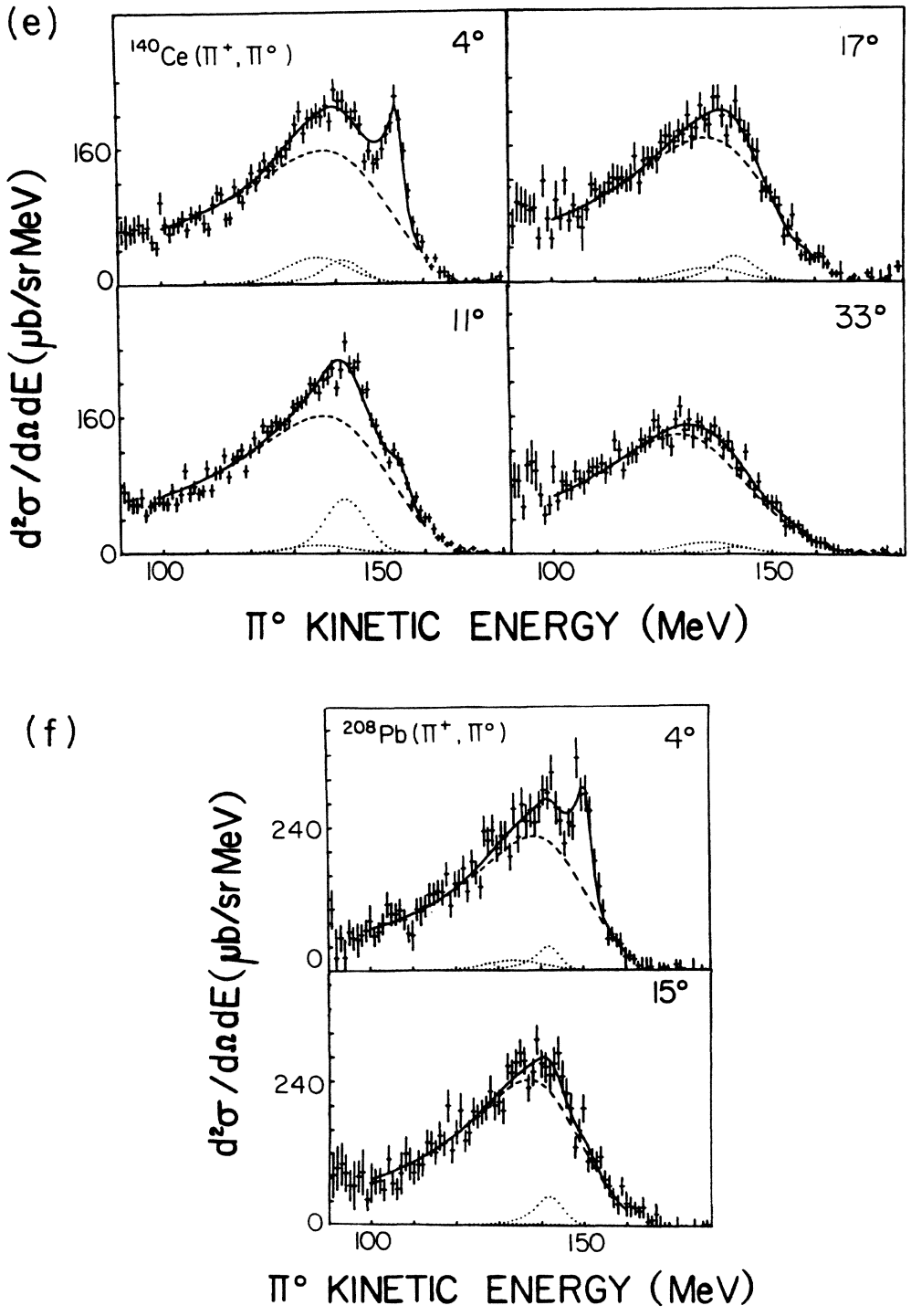

FIG. 6. (*Continued*).

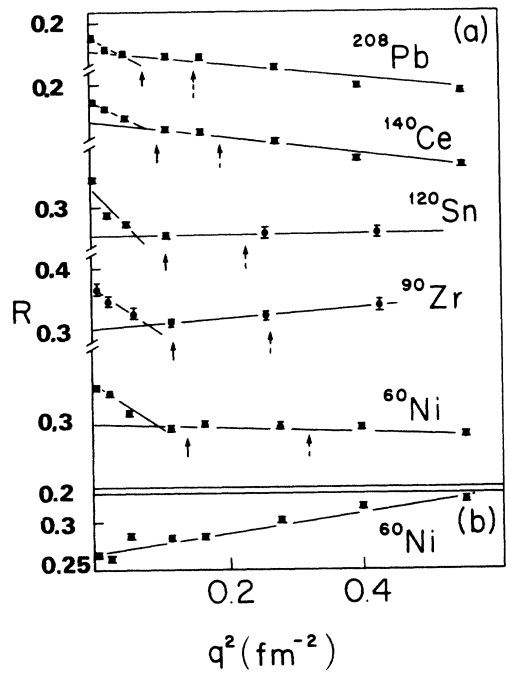

FIG. 7. (a) The ratio R between the cross section integrated over the expected monopole region to the cross section integrated over the whole spectrum, plotted vs q^2 for the (π^-,π^0) reaction on several nuclei. The arrows indicate the position of the expected first minimum of the IVM angular distribution. The lines represent linear fits to the points below and above the first minimum. The dotted arrows indicate the peak of the expected IVQ angular distributions. (b) The ratio R obtained for ^{60}Ni(π^-,π^0) for a region of excitation energies above the IVM expected position.

smooth ν dependence and an approximately linear q^2 dependence at each ν. Further discussion of the background is given in Sec. III B. For the IVM and GDR, the instrumental line shape, determined from the π^0 peak in the CH_2 data, was convoluted with a Gaussian resonance shape. As discussed below, the background function depends on a small dimensionless parameter, the momentum transfer q divided by the Fermi momentum k_F squared, $(q/k_F)^2$, and hence cannot have a rapid q^2 (angular) variation.

The background and resonance parameters for each nucleus were determined simultaneously by a least-squares fit of the data. In the first iteration the background parameters and the positions and widths of the resonances were determined. Since the GDR was unambiguously identified by its energy, and in order to minimize the uncertainty involved in the determination of the background, the GDR angular distribution was constrained to the DWIA shape (corrected for the finite acceptance of the spectrometer). Rather than also constraining the IVM angular distribution to the DWIA shape, its contribution was simply set to zero at angles larger than 15°, and the amplitudes in the three forward angles were taken as free parameters. In this way the data were not forced to produce an IVM signal by imposing the expected IVM angular distribution. The constraints of linearity in q^2 and smoothness in ν did not allow the background component to follow the rapid increase of the IVM cross section at forward angles. For those cases where the IVM strongly overlaps the GDR, the position of the latter was also constrained to the RPA energies and widths, which are consistent with other experimental data (see Fig. 15). The positions and widths of the resonances were kept fixed from angle to angle. The resulting parameters of the background varied smoothly from nucleus to nucleus. For the ^{120}Sn and ^{208}Pb(π^+,π^0) reactions, where no data above 15° (11° for ^{120}Sn) were available, some background parameters were interpolated or extrapolated from neighboring nuclei.

In the second iteration the only free parameters were the IVM and GDR amplitudes, and these were allowed to vary without constraint. The resulting angular distributions (plotted in Sec. IV A) are consistent with the DWIA angular distributions after adjustment of the magnitude. This agreement supports the correctness of the first iteration. In the π^+ data, the IAS peak partially overlaps the GDR and the least-squares fit included an IAS peak (with zero intrinsic width) at the known energy.[23] The dashed lines in Figs. 5 and 6 represent the resulting background, the dotted lines show the fit to the GDR and IVM resonances, and the solid lines give the fit to the sum. The normalized χ^2 values of the overall fits varied from 1 to 1.4.

B. Discussion of the nonresonant background

Our data show that the cross sections may be decomposed into a nonresonant background component, approximately linear in q^2 at fixed excitation energy, and giant resonances whose angular distributions vary relatively rapidly with q^2. This observed behavior is sufficient for separating the resonance signal from the background. It is nonetheless interesting to attempt a physical understanding of the nonresonant background. Data on inclusive pion charge exchange[24] and inelastic scattering[25] indicate that a large fraction of the cross section at large angles is due to the quasifree reaction. Our data at forward angles are in agreement with the plotted data. At these small angles Pauli blocking should strongly inhibit the quasifree charge exchange due to the small momentum transfer, consistent with data of Ref. 24. However, our data show that the broad structure of the background does shift with angle according to the free π-N kinematics even at small angles, indicative of the quasifree nature of at least part of the cross section. Such a process may proceed at small angles, in spite of the momentum mismatch, via high-momentum components of the nuclear wave functions.

Additional support for this hypothesis is given by the success of the pole approximation to describe radiative pion capture at small momentum transfers.[26] In this approximation the reaction is assumed to proceed through a collision with a single nucleon. The distortion due to the spectator nucleus, which partly accounts for multiple

scattering, is taken into account. The energy and angle dependences retain the general quasifree shape, but may shift from the exact free kinematics. The energy spectra in this case are surprisingly similar to the general shape of our background. We also mention in this context the semiphenomenological calculation of proton inelastic scattering at forward angles by Bertsch and Scholten.[27] They used a semi-infinite slab model for the nucleus, and showed that the single-step reactions constitute a large fraction of the total cross section. Due to the surface-peaked interaction, this component has a considerable contribution even for zero-degree scattering.

The size of the linear q^2 dependence of the background, which is small relative to the angular variation of the resonant cross sections, may be explained as a consequence of the background consisting of single-step (quasifree) or multiple-step knockout reactions. The giant resonance cross sections are surface related diffractive and the nuclear radius (R) sets the scale for the angular variation of the cross sections. Indeed, the giant resonance cross sections can be approximated by sums of squares of Bessel functions, $J_l^2(qR)$.[14,15] For the knockout reactions, on the other hand, the momentum transfer to the residual nucleus has an uncertainty of the order of the Fermi momentum (k_F) due to the momentum carried away by the unobserved knocked out nucleon, and hence the diffraction pattern is smeared out. In this case the q dependence of the cross section would scale with the Fermi momentum rather than with the nuclear radius. The cross section may then be expanded in a Taylor series in the dimensionless parameter $(q/k_F)^2$, since a cross section must be an even function of the scattering angle. In the angular range of the present experiment, $(q/k_F)^2<0.25$, so that terms higher than linear in q^2 are small. The fact that $(k_F R)^2 \gg 1$ (15 for medium nuclei) is therefore the reason for the approximately linear q^2 variation of the background in the very same region where the resonant cross sections fluctuate strongly. The preceeding arguments do not depend on the dominance of single-step processes. If multistep processes are important, the q^2 dependence will be further washed out.

For the quantitative analysis, we developed a semiphenomenological function to describe the doubly differential background cross section as a basis for a consistent treatment of the spectra for all targets and angles. In view of the above discussion, we adopted a function whose energy and angular dependence follow quasifree charge exchange at large momentum transfer, and which includes a suppression factor due to Pauli blocking. The semiphenomenological function, plotted schematically in Fig. 8, is given by

$$\frac{d^2\sigma}{d\Omega\, dE} = N \frac{1-e^{(E-E_0)/T}}{1+[(E-E_{\rm QF})/W_L]^2} \,. \tag{3.1}$$

The doubly differential background cross section is the product of three factors, a q dependent normalization N, a Lorentzian function of the π^0 energy E centered at an energy $E_{\rm QF}$ having a width W_L, and an energy cutoff factor with a maximum cutoff energy E_0 and a cutoff energy scale parameter T.

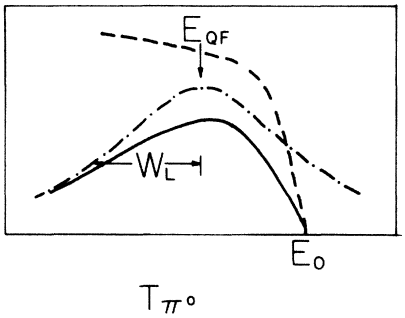

FIG. 8. The semiphenomenological background function. The double-differential cross section (solid line) is given by a product of a Lorentzian (dotted-dashed line), representing quasifree reaction, and an exponential cutoff (dashed line), which can be associated with the suppression due to Pauli blocking at forward angles.

The normalization N depends only on q and not on E. N is the product of three terms,

$$N = \frac{d\sigma}{d\Omega_0} A_0 \left[1 + A_1 \left[\frac{q}{k_F}\right]^2 + A_2 \left[\frac{q}{k_F}\right]^4\right] \times \left\{ \int \frac{1-e^{(E-E_0)/T}}{1+[(E-E_{\rm QF})/W_L]^2} dE \right\}^{-1} , \tag{3.2}$$

where $d\sigma/d\Omega_0$ is the cross section for the elementary charge-exchange process ($\pi^- p \rightarrow \pi^0 n$), the second term is a quadratic function of $(q/k_F)^2$, and the third term normalizes the energy integral of the E-dependent terms of $d^2\sigma/d\Omega\, dE$ to unity (see Table II). The energy integral is taken from $E=E_0-60$ MeV to $E=E_0$. The singly differential background cross section is given by

$$\frac{d\sigma}{d\Omega} = \frac{d\sigma}{d\Omega_0} A_0 \left[1 + A_1 \left[\frac{q}{k_F}\right]^2 + A_2 \left[\frac{q}{k_F}\right]^4\right] . \tag{3.3}$$

The Lorentzian may be associated with the π^0 energy in a quasifree reaction that is smeared out relative to the free π-N reaction, due to the Fermi energy of the struck nucleon. Therefore, its centroid $E_{\rm QF}$ was constrained to the

TABLE II. The momentum transfer q and the $\pi^- p \rightarrow \pi^0 n$ cross sections (Ref. 22) used in the definition (3.1)–(3.6). k_F was taken to be 297 MeV/c.

θ (deg)	q (MeV/c)	$(d\sigma/d\Omega)(\pi^- p \rightarrow \pi^0 n)$ (mb/sr)
4	27.4	10.0
7	33.5	9.86
11	47.8	9.58
15	67.0	9.1
17	82.0	8.78
22	106.2	7.99
28	126.4	7.17
33	149.0	6.23

expected mean π^0 energy of the quasifree charge exchange. For incident negative pions this energy was taken to be

$$E_{\rm QF}=T_{\pi^0}(\pi^-{\rm p}\rightarrow\pi^0{\rm n})-\text{neutron binding energy}\ , \quad (3.4)$$

where $T_{\pi^0}(\pi^-{\rm p}\rightarrow\pi^0{\rm n})$ is the π^0 energy in the free π-N reaction. The angular variation of T_{π^0} follows the nucleon recoil energy

$$T_{\pi^0}(q)=T_{\pi^0}(q=0)-q^2/2M\ , \quad (3.5)$$

where $q=2k_\pi\sin(\theta/2)$, M is the nucleon mass, and k_π is the momentum of the incident pion. For π^+, $E_{\rm QF}$ was set equal to

$$E_{\rm QF}=T_{\pi^0}(\pi^+{\rm n}\rightarrow\pi^0{\rm p})-{\rm CB}-\text{proton binding energy}\ . \quad (3.6)$$

CB is an additional free parameter required by the data, which may be associated with the Coulomb barrier for the struck proton. Following the linear q^2 assumption, the Lorentzian width was chosen as

$$W_L=W_{L_0}[1+\alpha(q/k_F)^2]\ , \quad (3.7)$$

with α and W_{L_0} taken as free parameters.

The exponential cutoff may be associated with effects of Pauli blocking and Fermi averaging of the π-N cross section: increasing suppression due to Pauli blocking and kinematics as a function of decreasing angle is provided by the function in Eq. (3.1) by the fact that the central energy of the Lorentzian shifts towards the cutoff energy (E_0) as the momentum transfer to the struck nucleon decreases; the π-N center-of-mass energy is a function of the initial direction of the struck nucleon in the quasifree reaction, resulting in an effective cross section that is a function of the energy of the outgoing π^0.[25] The exponential slope T is expected to be of the same size as the Fermi energy and it was set to a constant value that gave, on the average, the best fit to the data for all the reactions. The cutoff energy E_0 should lie in the vicinity of the residual-nucleus ground state. E_0 was a free parameter for each reaction, but was kept fixed from angle to angle.

A least-squares fit of the data for each nucleus to the sum of background, IVM, and GDR components was used in order to determine simultaneously the parameters in Eqs. (3.2)–(3.7), together with the resonance parameters. The best fit background parameters, listed in Table III, are approximately smooth as a function of the nuclear mass. The Lorentzian full width at half maximum ($2W_L$) is of the order of the Fermi energy, as is the parameter T. E_0 (column 8) is close to the ground states of the residual nuclei (column 11) and CB (column 7) is related to the Coulomb barrier (column 10). At an intermediate stage of the analysis procedure, the quantity M (the mass of the recoiling particle) in Eq. (3.5) was allowed to vary as a free parameter. The best fit to the data was obtained for a value of M within 10% of the nucleon mass, indicating that the broad structure of the background does shift with angle according to quasifree kinematics. The parameter A_0 is the ratio of the singly differential zero-degree cross section to the zero-degree cross section for the process $\pi^-{\rm p}\rightarrow\pi^0{\rm n}$. For the (π^+,π^0) data A_0 increases with the nuclear mass, whereas for (π^-,π^0) it is approximately constant. Similar behavior of the inclusive (π^+,π^0) cross sections was observed also at backward angles.[24] The difference between the π^- and π^+ A dependences of the cross sections in Ref. 21 was explained as being due to Pauli blocking of the protons [which are the interacting nucleon in the (π^-,π^0) case] and possibly also due to the screening of the protons by the excess neutrons.

In conclusion, the semiphenomenological function successfully describes the background in a consistent way for all targets and angles with a small number of parameters, which vary smoothly with atomic mass. Furthermore, some of these parameters may be given physical interpretations. The plausability of the background function contributes to the level of confidence in this analysis procedure. In the following error analysis, we estimate the extent to which the results for the resonances would vary if other shapes, which are not necessarily of quasifree nature, were assumed for the background.

We emphasize that our final results are not dependent on the specific parametrization of the background described above. The features that are used to separate the resonance signals from the background are the rapid q^2-dependent variation of the resonance angular distributions compared to the smooth q^2-dependent variation of the background.

C. Error analysis

The total errors have several sources. (I) Statistical errors: The error bars in Figs. 5 and 6 represent only the statistical errors and are relatively small. (II) 4% relative errors in the variation of the detection efficiency as a function of angle (see Sec. II). (III) 5% normalization errors due to the uncertainty in the π-N cross sections that were used for the solid angle calibration. (IV) Data taken at different rates showed that at high rates the detection efficiency was lowered and was target- and spectrometer-position dependent. The high-rate data were corrected for this effect, but there was still a 10% error for each measurement. In order to account for possible differences in the efficiency at the 5° and 25° spectrometer positions, the normalization of the 25° data was allowed to vary relative to that of the 5° data in the fitting procedure described in Sec. III A. The effect of this correction on the final results was small compared to the fitting errors, described below. (V) Uncertainty in the background determination (fitting errors): The largest contribution to the error comes from the fitting errors. We estimated to what extent the results for the resonances would vary if other background shapes were assumed that did not necessarily follow the quasifree description but were still approximately linear functions of q^2 at each excitation energy. For that purpose, the results were compared with a simpler analysis which had been previously used for the ^{120}Sn and ^{90}Zr data of limited angular range.[7] It follows from the linear q^2 assumption that the change in the background at the forward angles is small; making the extreme assumption that the background is isotropic up to

TABLE III. Results for the semiphenomenological background, defined in the relations (3.1)—(3.6). The values in parentheses for ^{120}Sn and ^{208}Pb were projected from neighboring nuclei. The two right-hand columns give the values of the Coulomb barrier and the expected position of the residual nucleus ground state in the energy spectra. Their values are close to the best fit values of the free parameters CB and E_0, respectively.

Target	A_0	A_1	A_2	W_{L0}	α	CB	E_0	T	Coulomb barrier	g.s. position
π^-										
^{40}Ca	0.492	2.14	0.61	21.7	0.0		165.7	70		166.3
^{60}Ni	0.613	2.80	0.20	21.1	1.0		165.6			165.0
^{90}Zr	0.531	0.74	0.35	20.2	0.0		166.5			166.0
^{120}Sn	0.539	1.05	0.90	21.6	0.1		163.2			163.0
^{140}Ce	0.534	2.53	0.97	21.3	2.1		165.5			164.0
^{208}Pb	0.519	3.43	−4.00	21.5	0.9		166.6			162.6
π^+										
^{40}Ca	0.394	5.46	10.4	22.7	1.2	7.0	159.7		6.4	155.5
^{60}Ni	0.710	2.81	3.0	23.1	−1.3	11.6	163.4		7.8	162.8
^{90}Zr	0.808	4.64	6.6	23.2	0.0	13.6	164.0		9.6	162.6
^{120}Sn	0.928	2.77	(6)	22.0	(0)	(13)	166.0		11.0	166.7
^{140}Ce	0.988	2.96	5.5	23.0	0.0	12.7	166.9		12.2	165.6
^{208}Pb	1.133	3.39	(6)	18.3	(0)	12.7	165.7		15.0	165.8

$\theta = 15°$, one can extract the resonance properties in this angular range by simply subtracting spectra at different angles. Thus the 11° spectra, where the IVM cross section is expected to be small, were subtracted from the 4° spectra where it is near its maximum. The resulting 4°—11° difference spectra were fitted to a sum of positive (IVM, and also IAS in the π^+) and negative (GDR) peaks. The energies and widths of the resonances were generally not constrained. The 4°—11° difference spectrum for the reaction ^{120}Sn(π^-,π^0) clearly demonstrates the presence of an IVM signal, as shown in Fig. 10. Subsequently, the 7°—11° and 15°—11° difference spectra were fitted to the IVM and GDR peaks, fixing their energies and widths to the 4°—11° results and allowing only their amplitudes to vary. The difference cross sections deduced from the peak areas were fitted to the corresponding normalized DWIA difference cross sections,[6] corrected for the finite acceptance of the spectrometer. The experimental peak cross sections then were derived as described in Sec. IV A.

The low-energy tail of the background is observed in the π^- data to increase by up to 10% going from 4° to 15°, in contradiction to the assumption of isotropy. The increase of the background appears in Fig. 9 as the negative cross section below 130 MeV. This has a particularly strong effect on the results for the IVM in ^{40}Ca and in all the π^+ data, where the IVM is broad and is located at the low-energy tail. We plot in Fig. 10(a) the 4°—11° difference spectrum for ^{60}Ni(π^+,π^0), showing too much subtraction of background below 120 MeV and the weakening of the IVM signal. Thus, to extract the IVM fitting errors in those reactions, the 4°, 7°, and 15° bins were first normalized to the 11° cross section in a 20-MeV region of excitation energies above the IVM and then subtracted. Figure 10(b) shows the resulting 4°—11° spectrum for ^{60}Ni(π^+,π^0), with a clear IVM signal. For the GDR and IAS parameters we used the simple subtraction method [Fig. 10(a)].

The fitting errors were estimated from the differences between the subtraction and full analyses, requiring a smooth A dependence of the errors. The π^+ results have larger fitting errors than those for π^-, for several reasons. The IVM, excited by (π^+,π^0), lies at a higher excitation energy and therefore has a larger width and a smaller resonance to background ratio. The GDR is larger and wider and overlaps more strongly with the IVM, and the IAS in the π^+ spectra also overlaps with the GDR. Further-

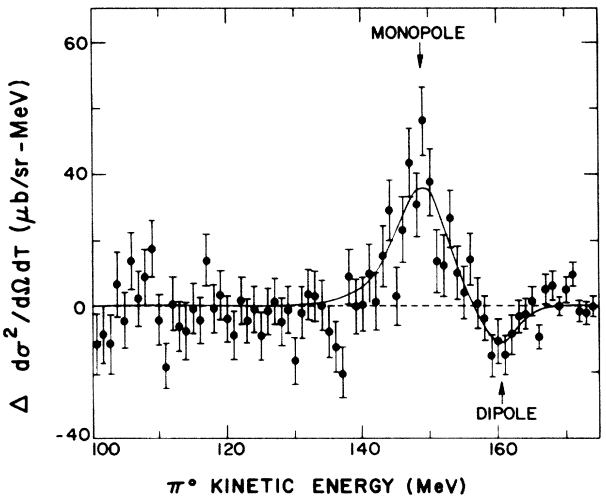

FIG. 9. ^{120}Sn(π^-,π^0) difference spectrum: 4° minus 11°. The line represents a fit to the sum of positive (IVM) and negative (GDR) peaks. This analysis was carried out only for the purpose of estimating the fitting errors.

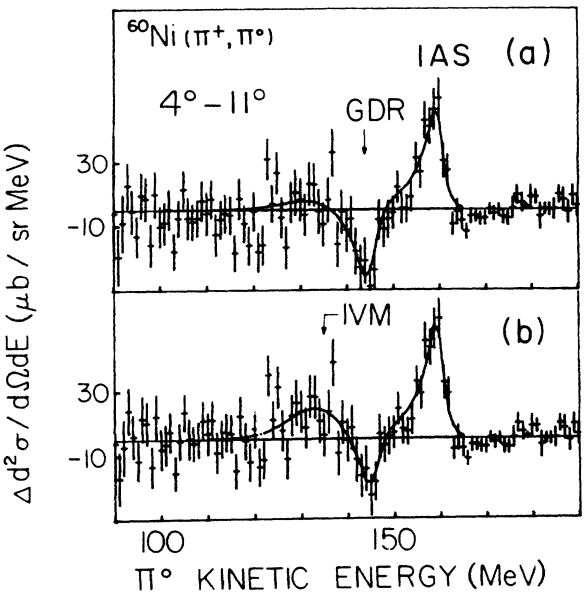

FIG. 10. The ^{60}Ni(π^+,π^0) difference spectra of 4° minus 11°, (a) without relative normalization and (b) with a normalization of the 4° spectrum to match the 11° cross section below 120 MeV. The lines represent fits to the sum of positive (IVM and IAS) and negative (GDR) overlapping peaks. The IVM parameters were extracted from spectra like the one shown in (a), whereas the GDR and IAS parameters were extracted from spectra like the one in (b). This analysis was carried out only for the purpose of estimating the fitting errors.

more, the background is larger, especially for the heavier nuclei. For these reasons, and especially due to the larger overlap of the IVM and GDR, the errors of the IVM cross sections for ^{120}Sn, ^{140}Ce, and ^{208}Pb(π^-,π^0) are of the order of the cross sections themselves. The errors for the widths and energies of the IVM in the ^{140}Ce and ^{208}Pb(π^-,π^0) data are also rather large, due to the fact that the IVM lies in a region where the background varies strongly as a function of energy.

The IAS energy was also determined in the subtraction analysis in order to serve as an additional test of the analysis procedure. The resulting values for this parameter are no more than 0.7 MeV away from the predicted energies. Such small deviations may be due either to fitting or to calibration errors. Considering the second possibility, a systematic error of 0.7 MeV was assigned to the IVM and GDR excitation energies in addition to the statistical and fitting errors.

IV. RESULTS

A. IVM and GDR

The angular distributions for the IVM and GDR are shown in Fig. 11. The data points represent differential cross sections averaged over the finite range of the angular bins. In order to compare the data to RPA-DWIA angular distributions,[6] the theoretical cross sections were folded with the finite angular acceptance and multiplied by normalization factors to fit the data. The finite angular acceptance corrections were made with the approximate relation

$$\frac{d\sigma}{d\Omega_{\text{corrected}}} = \frac{d\sigma}{d\Omega} + \tfrac{1}{2}\sigma_\theta^2 \frac{d^2}{d\theta^2}\left[\frac{d\sigma}{d\Omega}\right], \tag{4.1}$$

where the $d\sigma/d\Omega$ are the theoretical values, the $(d^2/d\theta^2)(d\sigma/d\Omega)$ are the curvatures of the calculated angular distributions, and the σ_θ^2 are the standard deviations of the angular acceptance, given in Table I. The solid lines in Fig. 11 connect the theoretical cross sections obtained in this manner. The numbers given in column 3 of Table IV are the RPA-DWIA peak cross sections (at 0° for the IVM and around 15° for the GDR) multiplied by the normalization factors. Such a procedure has only a

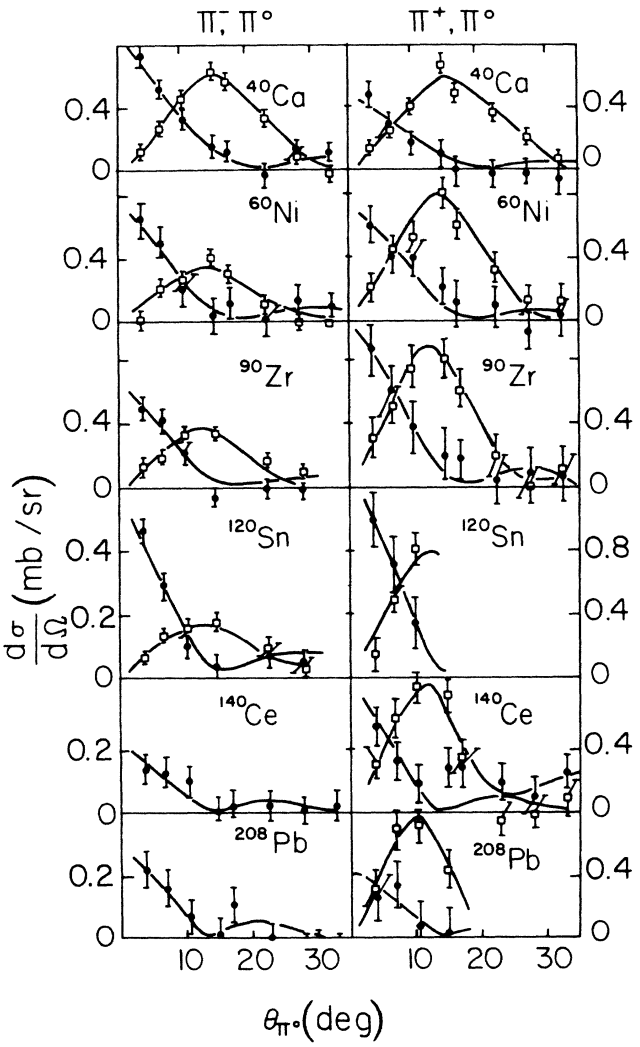

FIG. 11. Angular distributions for the IVM and GDR. The data points represent cross sections averaged over the approximately 5° range of the angular acceptance. The lines represent DWIA calculations corrected for the finite acceptance and normalized to the data. Error bars do not include fitting errors.

TABLE IV. Peak differential cross sections, excitation energies, and widths for the IVM and GDR. The peak cross sections were extrapolated from the angular distributions in Fig. 11 using the DWIA shapes. The excitation energies are relative to the ground states of the target nuclei. The excitation energies E_x satisfy the relationship $W_{in}=E_x+W_{out}$, where W_{in} and W_{out} are the total energies, kinetic plus mass, of the incoming and outgoing pions. The widths correspond to the full width at half maximum (FWHM) of the fitting Gaussian resonance shape. A 10% normalization error and a 0.7 MeV energy calibration error should be added for each reaction independently. The GDR energies and widths given in parentheses could not be extracted from the data due to the strong overlap with the IVM, and were constrained to the RPA values.

Reaction	Resonance	Peak cross section (μb/sr)	Excitation energy (MeV)	Width (MeV)
$^{40}Ca(\pi^-,\pi^0)$	IVM	768±200	24.1±1.5	21.6±1.9
	GDR	856±87	13.8±1.6	5.7±2.3
$^{40}Ca(\pi^+,\pi^0)$	IVM	533±220	35.9±2.9	24.2±4.0
	GDR	725±126	24.7±2.1	6.4±1.9
$^{60}Ni(\pi^-,\pi^0)$	IVM	725±185	25.2±1.7	14.7±2.1
	GDR	358±75	13.5±1.6	4.2±2.0
$^{60}Ni(\pi^+,\pi^0)$	IVM	704±280	35.6±2.8	18.4±4.1
	GDR	792±190	25.3±1.5	6.4±1.7
$^{90}Zr(\pi^-,\pi^0)$[a]	IVM	632±143	22.0±2.0	15.0±2.1
	GDR	392±61	10.4±1.8	2.7±1.4
$^{90}Zr(\pi^+,\pi^0)$[b]	IVM	1040±300	34.6±2.9	18.9±4.1
	GDR	912±272	25.7±1.2	6.0±1.7
$^{120}Sn(\pi^-,\pi^0)$[a]	IVM	532±108	21.4±2.2	9.2±2.6
	GDR	193±46	9.6±1.8	(0)
$^{120}Sn(\pi^+,\pi^0)$	IVM	1277±1110	30.0±3.0[c]	16.0±4.1
	GDR	858±335	23.9±0.9	3.4±2.1
$^{140}Ce(\pi^-,\pi^0)$	IVM	228±103	19.9±2.4	8.5±4.5
$^{140}Ce(\pi^+,\pi^0)$	IVM	727±720	35.4±3.5[c]	16.6±4.2[c]
	GDR	815±357	(25.3)	(8)
$^{208}Pb(\pi^-,\pi^0)$	IVM	309±87	12.0±2.8	11.6±7.1
$^{208}Pb(\pi^+,\pi^0)$	IVM	466±460	37.2±3.5[c]	15.0±6.0[c]
	GDR	843±450	(26.5)	(6)

[a]The results for ^{120}Sn,$^{90}Zr(\pi^-,\pi^0)$ are slightly different from those published earlier (Ref. 7). The data in both cases were the same; the small differences are due to the improved analysis used in the present work.

[b]Due to an ambiguity in the normalization of the $^{90}Zr(\pi^+,\pi^0)$ data, we cannot exclude the possibility that the cross sections for this reaction may have been overestimated by up to 40%.

[c]These results are not determined as well as in the other cases because the cross sections themselves are consistent with zero.

weak model dependence, since at the small angles considered here the shapes of the theoretical angular distributions are sensitive neither to the nuclear structure input nor to the higher-order terms of the interaction. The errors in Fig. 11 consist of the statistical errors added in quadrature to the relative-efficiency errors. The fitting errors only had a small effect on the shape of the angular distributions and therefore were not included in the figure. Several data points have negative values, corresponding to an overestimate of the background, but they are all statistically consistent with zero.

In order to test the extent to which the pion-nucleus interaction radius (R) was consistent with the values extracted from elastic scattering, the angular distributions were also fitted to the simple diffractive scattering relations[14] $\sigma J_l^2(qR)$ corrected for the finite angular acceptance. The J_l's are Bessel functions with $l=0$ for the IVM and $l=1$ for the GDR. The pion interaction radius

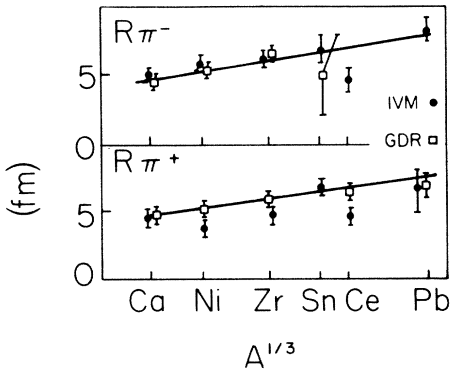

FIG. 12. Pion interaction radii (R) extracted by fitting the angular distribution in Fig. 11 to the diffractive relations $J_l^2(qR)$. The straight lines connect the values extracted from π^+ and π^- elastic scattering at 180 MeV.

R and maximum cross sections σ were free parameters. We note that the shapes of the diffractive angular distributions with radii extracted from elastic scattering are similar to those of the DWIA calculations. The extracted radii are plotted in Fig. 12 versus $A^{1/3}$. They lie approximately on the same straight line that fits the π^+ and π^- elastic scattering data at 3,3 resonance energies.[28]

The experimental results for the IVM and GDR are summarized in Table IV (for graphical presentation, see Sec. V). The fitting errors are included. Absolute normalization errors of 10% and 0.7-MeV calibration errors should be added independently for each target and beam polarity. Due to an ambiguity in the normalization of the $^{90}Zr(\pi^+,\pi^0)$ data, we cannot exclude the possibility that the cross sections for these reactions may have been overestimated by up to 40%. The GDR cross sections are given for all the π^+ reactions, and for the π^- reactions only in the lighter targets. The IVM cross sections are given for all the π^- reactions and for π^+ for the light targets only. For the π^+ reactions on ^{120}Sn, ^{140}Ce, and ^{208}Pb the IVM properties could not be unambiguously determined. Due to the large fitting errors the cross sections are consistent with zero as well as corresponding to a large fraction of the theoretical values. The width of the weak GDR in the $^{120}Sn(\pi^-,\pi^0)$ reaction could not be determined from the data and was fixed in the fitting process to the RPA value. For the ^{140}Ce and $^{208}Pb(\pi^+,\pi^0)$ analysis, where the GDR overlaps the broad IVM, the GDR energies and widths were also fixed to the RPA values.

B. Isovector quadrupole

The data analysis did not require an isovector quadrupole (IVQ) component, although the angular range of the measurements extends well beyond the second maximum of the calculated IVQ angular distribution. The RPA calculations,[6] which give a good description of the IVM and GDR, predict a concentration of isovector $E2$ strength. Therefore we searched for an IVQ resonance having the RPA energies and widths. The search was conducted only for the π^- data, where the fitting errors for the IVM and GDR were relatively small. The data were fitted to a sum of background, IVM, GDR, and IVQ components. The background parameters as well as the IVM and GDR positions and widths were allowed to vary. The angular distributions of all three resonances were assumed to have the DWIA shapes (corrected for the finite angular acceptance of the spectrometer). The calculated IVQ angular distribution $(d\sigma/d\Omega)(\mathrm{IVQ})$ is relatively flat (see Fig. 2) and it is therefore difficult to distinguish an IVQ signal from the background. In order to estimate the fitting errors, we made the extreme assumption that any part of the IVQ angular distribution that is linear in q^2 could be hidden in the background. Therefore, the search was carried out using a trial function that was a sum of the calculated IVQ angular distribution and a function linear in q^2:

$$\frac{d\sigma}{d\Omega}=\lambda\frac{d\sigma}{d\Omega}(\mathrm{IVQ})+A+B(q/k_F)^2 . \tag{4.2}$$

Here, λ, A, and B are free parameters. This analysis for the IVQ is free of assumptions about the background beyond its approximately linear q^2 dependence. The error in λ reflects both statistical and fitting errors, and was used to determine the error in the IVQ cross sections. Large values for A or B imply distortion of the smooth energy dependence of the background. Therefore, this analysis was used only to extract the errors in the IVQ cross sections and not their central values.

Table V summarizes the results. The peak IVQ cross sections are given in column 2, and ratios of the deduced 90% confidence upper limits to the RPA-DWIA values appear in column 3. Columns 4 and 5 give the RPA energies and widths that were used as constraints in the fit. The widths were estimated from the RPA $E2$ strength distributions. In column 6 we give the cross sections that were obtained when the IVQ was assumed to have twice the RPA width. The upper limits do not change considerably if we search for the IVQ a few MeV away from the predicted positions. The method of analysis described in this section gives results for the IVM and GDR that are consistent with the previous analysis (Sec. IV A).

TABLE V. This table gives the upper limits for the IVQ cross sections in the (π^-,π^0) reactions. The peak differential cross sections are given in column 2. The rations of the deduced 90% confidence upper limits to RPA-DWIA values are given in column 3. Columns 4 and 5 give the RPA energies and widths that were used in the fit. The values in column 6 were obtained assuming that the IVQ has twice the RPA widths.

Target	Peak cross section (μb/sr)	Upper limits RPA-DWIA	RPA excitation energy (MeV)	RPA width (MeV)	2×RPA width section (μb/sr)
^{40}Ca	23±60	0.18	26.4	10	110±72
^{60}Ni	0±80	0.30	25.1	7	0±95
^{90}Zr	1±50	0.15	20.9	6	1±120
^{120}Sn	37±85	0.64	19.3	4	0±95
^{140}Ce	0±20	0.16	18.9	3	0±40
^{208}Pb	21±70	1.50	13.4	2	21±75

V. COMPARISON WITH THEORY AND WITH OTHER DATA

The properties of $L=0$, 1, and 2 isovector resonances were calculated by Auerbach and Klein[6] for all the target nuclei. The strength distributions and the transition densities were treated in the Hartree-Fock–RPA framework, and subsequently, the $\pi^{\pm}$ cross sections were calculated in the DWIA. Two methods of calculations were used. Method IV calculates energy-dependent transition densities and derives double-differential cross sections. The average excitation energies are defined as the first moment of the double-differential cross sections. In method III the average energy is defined as the first moment of the multipole transition strength distribution; average transition densities and differential cross sections are derived assuming that all the strength is concentrated at the average energy. In principle, method IV is more nearly correct, but it is also more sensitive to the nuclear structure input. The mean energies calculated in method III correspond to the usual definition of the excitation energies of giant resonances, whereas the ones derived in method IV correspond to the measured energies. Clearly, differences between the two depend on the reaction model used.

At the 3,3 resonance, the angular dependence of the DWIA $(\pi^{\pm},\pi^0)$ angular distributions are not sensitive to the difference between the two methods and they resemble the expected diffractive $J_l^2(qR)$ patterns,[14,15] where R is the pion-nucleus interaction radius. The magnitude of the cross sections is sensitive mainly to the transition density at large radii, because of the strong absorption of the pions. For the IVQ cross sections, methods III and IV give similar results. The values quoted in Table V correspond to method IV.

The same RPA-DWIA calculations were carried out for the IAS.[29] For this narrow state the differences between methods III and IV are negligible and the data[18] have relatively small fitting errors. The measured cross sections exhaust, on the average, 120% of the RPA-DWIA estimates, which gives a measure for the reliability of the calculations.

The RPA calculations in Ref. 6 couple 1p-1h configurations to the continuum but not to multiparticle-hole excitations. The additional width due to the mixing of 2p-2h configurations was calculated by Adachi and Auerbach[30] for the $T+1$ IVM in target nuclei heavier than ^{60}Ni.

Figures 13 and 14 compare our data to the RPA calculations. The lines in panel (c) for the IVM in the ^{90}Zr, ^{120}Sn, ^{140}Ce, and ^{208}Pb(π^-,π^0) reactions connect the points calculated by Adachi and Auerbach. For the other cases, the lines represent estimates from the double-differential cross sections in Ref. 6. We note that the calculated cross sections are fragmented. The effective widths were estimated by fitting the theoretical double-differential cross sections to Gaussian shapes. This procedure is similar to the data analysis that assumed Gaussian shapes for the resonant peaks.

In Fig. 14 the energies and widths of the GDR are compared with results from (p,n) (Ref. 31), (γ,n) (Ref.32),

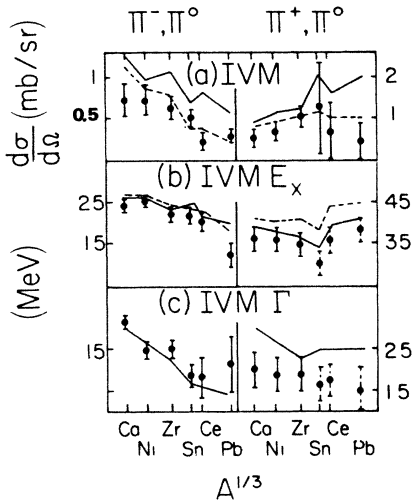

FIG. 13. (a) IVM peak cross section, (b) excitation energies, and (c) widths. The energies are relative to the ground states of the target nuclei. The dashed error bars indicate that the excitation energies and widths are not determined as well as in the other cases (see text). The lines in (a) and (b) connect the RPA values, method III (dashed line), and method IV (solid line). The lines in (c) represent calculations for ^{90}Zr, ^{120}Sn, ^{140}Ce, and ^{208}Pb(π^-,π^0) that include mixing of 2p-2h configurations, and for the other cases estimates from double-differential cross sections (Ref. 6) that do not include such mixing. See comment on ^{90}Zr(π^+,π^0) and additional normalization and calibration errors in Table V.

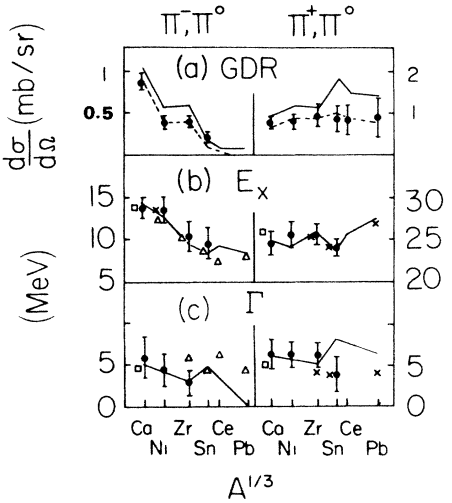

FIG. 14. GDR peak cross sections, excitation energies, and widths. The lines connect the RPA values from Ref. 6, method III (dashed line), and method IV (solid line). Other data on the excitation energies and widths are shown for comparison. The $\times$'s correspond to (p,n) (for π^+) and (n,p) data (for π^-). The squares represent the expected energies of the analogs of the GDR observed in ^{40}Ca(γ,n) reactions and the triangles the analogs of the $T+1$ GDR, excited by (γ,p) and (p,γ_0) reactions. See comment on ^{90}Zr(π^+,π^0) and additional normalization and calibration errors in Table V.

(γ,p) (Ref. 33), (p,γ_0) (Ref. 34), (γ,γ) (Ref. 35), and (n,p) (Ref. 36) reactions. The (p,n) data were obtained with low-energy protons that mainly excite the $T-1$ component of the non-spin-flip GDR, in contrast to (p,n) at higher energies that favor the spin-flip dipole. The (γ,p), (p,γ_0), and—in ^{40}Ca—also the (γ,n) reactions excite the analog of the $T+1$ GDR reached by (π^-,π^0) (see Fig. 1). The points in Fig. 14(b) were obtained using Coulomb displacement from Ref. 23. The states excited by (π^-,π^0) are expected to have smaller widths than their photonuclear analogs due to their lower excitation energies in the residual nuclei.

VI. DISCUSSION

The observed properties of the IVM and GDR resonances agree with several model independent predictions. Figure 11 demonstrates the quality of the fits of the experimental cross sections to the shapes of the DWIA angular distributions, and Fig. 12 shows that the strong absorption radii extracted from the IVM and GDR angular distributions are consistent with those extracted from $\pi^{\pm}$ elastic-scattering data. The IVM angular distribution is forward peaked and can be distinguished unambiguously from $L=1$ or 2 angular distributions. The ratio of the experimental to RPA-DWIA cross sections measures the extent to which the sum rule is exhausted. Both IVM and GDR exhaust approximately 60% of the RPA-DWIA method IV calculations and 100% of the method III calculations, indicating the collectivity of the resonances. The experimental cross sections for the $T+1$ components of the IVM and GDR decrease with increasing isospin of the target nuclei, which is not observed for the $T-1$ component with π^+ data, demonstrating the expected effect of Pauli blocking (see Figs. 13 and 14). The effect is stronger for the GDR than for the IVM since the excitations are $1\hbar\omega$ for the GDR and $2\hbar\omega$ for the IVM. In the ^{140}Ce and ^{208}Pb(π^-,π^0) reactions the GDR was not observed at all.

The comparison of experimental and theoretical excitation energies is of considerable interest. The excitation energies of the $T+1$ IVM are approximately 2 MeV below, and the $T-1$ IVM energies are 2–4 MeV below, the RPA (method IV) values. Such small differences can be due to mixing with multiparticle-hole states, which were not taken into account by Auerbach and Klein, and which can cause a reduction in the centroid of the order of the added decay width.[37] The effect for the $T-1$ state will be larger than that for the $T+1$ state because of the higher density of states at the higher excitation energy of the $T-1$ state. The widths of the $T+1$ IVM are in good agreement with the RPA. They decrease with increasing mass, in accordance with the lower excitation energies in heavier nuclei. The observed widths of the $T-1$ states are narrower than the RPA values by one to two standard deviations. It is possible that the Skyrme III interaction used in the RPA gives too much fragmentation, which is known to occur for the GDR (see Fig. 14 for the comparison of the RPA $T-1$ widths with existing data).

A comparison of the resonances excited by (π^-,π^0) and (π^+,π^0) yields information on the isospin splitting. Although the state excited by (π^+,π^0) is a mixture of the $T+1$, T, and $T-1$ components, in neutron-rich nuclei the transitions to the higher isospin states are weaker and it is a good approximation to attribute all the observed strength to the $T-1$ component. In these cases, the $T+1$, $T-1$ splitting can be deduced from the relation

$$\Delta(T+1,T-1)=E_x(T+1)-E_x(T-1)+\Delta E_C(Z_<)+\Delta E_C(Z_>)-2\Delta M_{\rm np}\ , \tag{6.1}$$

where the E_x are the mean energies of the $T+1$ and $T-1$ strength distributions, $\Delta E_C(Z_<)$ and $\Delta E_C(Z_>)$ are the Coulomb-displacement energies between the target nucleus Z to the $Z-1$ and $Z+1$ neighboring nuclei, and $\Delta M_{\rm np}$ is the neutron-proton mass difference (see Fig. 1). The E_x correspond to the mean energies calculated in the RPA method III calculations, whereas the experimental energies correspond to the mean energy of the double-differential cross section as defined in method IV. The E_x were deduced from the data using the differences between methods III and IV,

$$\begin{aligned} E_x(t_+)&=E(\pi^-)+E_{\rm III}(T+1)-E_{\rm IV}(T+1)\ ,\\ E_x(t_-)&=E(\pi^+)+E_{\rm III}(T-1)-E_{\rm IV}(T-1)\ , \end{aligned} \tag{6.2}$$

where $E(\pi^{\pm})$ are the measured energies. The Coulomb-displacement energies were taken from Ref. 23. The results for the IVM are given in column 4 of Table VI. We note that for $T=2$, ^{60}Ni, the measured splitting is smaller than the actual one, since, in addition to the $T-1$ state, the T component also contributes substantially to the (π^+,π^0) cross section.

A general treatment of isospin splitting in terms of isovector and isotensor potentials[38] gives the following relations for the $T+1$, $T(\Delta E_+)$ and $T,(T-1)(\Delta E_-)$ splittings:

$$\begin{aligned} \Delta E_+&=T+1[E_v+(2T-1)E_t]\ ,\\ \Delta E_-&=T[E_v-(2T+3)E_t]\ . \end{aligned} \tag{6.3}$$

TABLE VI. Isospin splitting between the $T+1$ and $T-1$ components of the IVM. Column 2 gives the splitting obtained when the measured (π^-,π^0) and (π^+,π^0) energies are identified with the $T+1$ and $T-1$ IVM, respectively. Column 3 gives our estimates for the splitting between the mean energies of the $T+1$ and $T-1$ strength distributions, based both on our data and the differences between the RPA method III and method IV calculations (see text). Column 4 gives the vector contribution to the symmetry potential, deduced from the splitting in column 3, multiplied by the nuclear mass.

Target	$E_x(\pi^-)-E_x(\pi^+)+2(\Delta E_C-\Delta m_{\rm np})$ (MeV)	$\Delta(T+1,T-1)$ (MeV)	AE_v (MeV)
^{60}Ni	5.6±3.3	4.4±3.3	53±40
^{90}Zr	8.4±3.0	5.2±3.0	43±25
^{120}Sn	15.9±3.3	12.4±3.3	71±19
^{140}Ce	12.1±4.2	8.8±4.2	49±24
^{208}Pb	9.6±4.5	5.1±4.5	24±21

Calculations[39] predict that for collective states the vector potential E_v multiplied by the nuclear mass is smaller than the single-particle symmetry potential of 100 MeV.[40] For the GDR, data on both ΔE_+ and ΔE_- in nuclei from ^{90}Zr to ^{208}Pb give $E_v A = 50$–70 MeV and less than 1 MeV for the tensor potential E_t.[31] We derived the vector potential for the IVM from the relation

$$\Delta(T+1, T-1) = \Delta E_+ + \Delta E_- = (2T+1)E_v - (T+1)E_t \ , \tag{6.4}$$

using the small values for the tensor potential E_t from Ref. 31. The resulting values for $E_v A$ are given in Column 5 of Table VII. They are generally of the order of 50 MeV, similar to those of the GDR.

The energies and widths of the GDR $T+1$ and $T-1$ components are in good agreement with the RPA and with other data (Fig. 14). The individual ΔE_+ and ΔE_- splittings were deduced using data from (p,n) reactions[32] for the energies of the GDR T component. The differences between the mean energies of the strength and the cross-section distributions were taken into account as described for the IVM. For the narrow GDR these corrections were small, within the range 0.5–1 MeV. The results for the isospin splittings of the GDR and the deduced vector potential are given in Table VII, where the above note for ^{60}Ni applies here as well. The results from Ref. 31 are given in column 5 for comparison. We note that although the errors are large, $(\pi^{\pm},\pi^0)$ may have some advantages in these derivations over the other reactions since both ΔE_+ and ΔE_- are measured with the same reaction mechanism.

The IVM and GDR excited by ^{40}Ca(π^-,π^0) are analogs of the resonances excited by ^{40}Ca(π^+,π^0). The measured energy shifts are 12.1 ± 3.3 MeV for the IVM and 10.9 ± 1.6 MeV for the GDR, in good agreement with the 12 MeV expected from the Coulomb displacement energies. The $T_z = \pm 1$ components of the IVM have comparable widths as expected, 21.6 ± 1.9 for (π^-,π^0) and 24.2 ± 4.0 for (π^+,π^0).

Unequal (π^+,π^0) and (π^-,π^0) cross sections for isovector resonances on $T=0$ targets can be expected if the neutron and proton ground-state densities are not the same. The resonance energy (π^-,π^0) reaction samples the surface proton density and the (π^+,π^0) reaction samples the surface neutron density. The Coloumb force causes the surface proton density to be larger than the surface neutron density in a $T=0$ nucleus. One therefore expects the (π^-,π^0) cross sections to be larger than the (π^+,π^0) cross sections. The experimental ratios of π^- to π^+ cross sections are 1.44 ± 0.15 for the IVM and 1.18 ± 0.28 for the GDR. Auerbach[41] calculates ratios of 1.45 and 1.40, respectively, by assuming (based on Hartree-Fock calculations) that the proton rms radius is 0.05 fm larger than the rms radius of the neutron. Unfortunately, the large errors in the experimental ratios do not allow a quantative test of the calculation.

Earlier[17] we published a ratio of 1.7 ± 0.2 for the GDR cross section in ^{40}Ca$(\pi^{\mp},\pi^0)$. That result was obtained with an analysis of a subset of the data, which achieved better energy resolution, but was not as complete as the present analysis. The earlier analysis assumed a strictly isotropic background and thus fitting errors were not included and, in addition, the IVM was not taken into account. We believe, therefore, that the present analysis gives more accurate results for the cross sections. The better resolution ^{40}Ca π^+ data suggested a possible broadening of the GDR, particularly noticeable at 22° and 28°, and it was suggested[17] that this broadening could be due to spin-flip resonances. The present analysis, which emphasized the IVM, compromised good resolution in favor of better statistics and assumed a constant width for the GDR. Therefore it was not sensitive to such a possible broadening.

Although the excitation energy of the IVM in the inelastic-scattering channel (T_0) was not measured directly in this experiment, it can be deduced on the basis of the $(\pi^{\pm},\pi^0)$ results for the $T+1$ and $T-1$ channels. The resonance in the T_0 channel is the one whose energy has been predicted by the hydrodynamical model[4] and which, in the case of the GDR, has been the most thoroughly studied. We used a simple approximation for the average energy of the T_0 strength,

$$E_x(T_0) = [E_x(T+1) + E_x(T-1)]/2 \ , \tag{6.5}$$

that neglects the differences between the $\Delta E_C(Z_<)$ and $\Delta E_C(Z_>)$ Coulomb energies and between ΔE_+ and ΔE_-. Substituting the π^- and π^+ results for $E_x(T+1)$ and $E_x(T-1)$, respectively, we obtain the values plotted in Fig. 15. Two cautionary remarks should be made regarding the validity of these estimates: (1) the values of the (π^+,π^0) energies in the heavy targets are not as well determined as in the other cases, and therefore the error bars for ^{120}Sn, ^{140}Ce, and ^{208}Pb in Fig. 15 may have been underestimated, and (2) we chose to make no model-dependent correction of the type made in Eq. (6.2). Thus, the values in Fig. 15 correspond to the mean energy of the double-differential cross sections rather than to the mean of the transition strengths, which is the usual definition of the excitation energy. Based on Eq. (6.2), we estimate that the mean energy of the strength distributions could lie approximately 2 MeV above the plotted values. The width of the IVM in the inelastic scattering channel may be estimated in a way equivalent to the approximation in (6.4). The results vary from 16 MeV in ^{60}Ni to 8 MeV in ^{208}Pb.

TABLE VII. Isospin splitting of the GDR $T+1$, T (ΔE_+), and T, $T-1$ (ΔE_-) components, and the resulting symmetry potential E_v multiplied by the nuclear mass. The energies of the $T+1$ and $T-1$ states are from this experiment, while the energies of the T components were taken from (γ,n) data.

Target	ΔE_+ (MeV)	ΔE_- (MeV)	AE_v (MeV)	AE_v [a] (MeV)
^{60}Ni	4.1 ± 1.6	1.0 ± 1.5	50.4 ± 25	
^{90}Zr	3.8 ± 1.8	1.8 ± 1.2	46.0 ± 17	51
^{120}Sn	6.4 ± 1.8	3.9 ± 0.9	58.4 ± 11	53
^{140}Ce				54
^{208}Pb				73

[a]Reference 2.

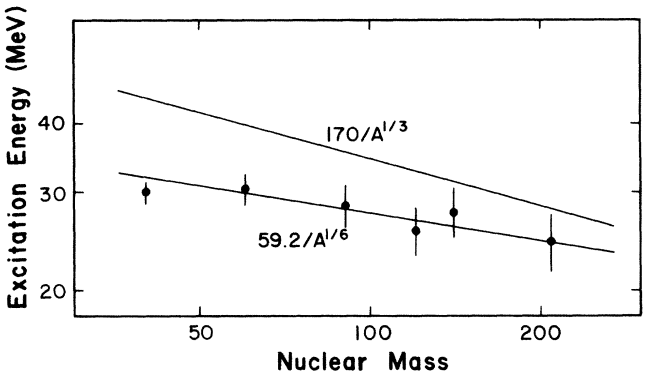

FIG. 15. Estimates of the IVM excitation energy in the inelastic-scattering channel, obtained by taking the average of the IVM energies in the (π^-,π^0) and (π^+,π^0) reactions. These values correspond to the mean energies of the double-differential cross sections. We estimate that the mean energy of the strength distributions could lie approximately 2 MeV higher. Due to the large ambiguity in the results for the heavy elements, the values for ^{120}Sn, ^{140}Ce, and ^{208}Pb are not as well determined as in the other cases. The solid line is a best fit to an $A^{-1/6}$ dependence, with a coefficient of 59.2±2.6 MeV. The function $170A^{-1/3}$ MeV is plotted as a dashed line.

The values in Fig. 15 come out considerably below the hydrodynamical prediction of Bohr Mottelson[1] of $170A^{-1/3}$ MeV, plotted in the figure. This resembles the situation of the GDR photonuclear data,[42] which seem to depend on $A^{-1/6}$ rather than on $A^{-1/3}$. The latter relation is a consequence of the Steinwedel-Jensen[43] model of volume oscillations, while the former has been predicted by Goldhaber and Teller[44] for surface oscillations. We find that the IVM excitation energies, plotted in Fig. 15, also depend on $A^{-1/6}$, with a coefficient of 59.2±2.6 MeV. It would be interesting to investigate theoretically whether this result can yield any specific information on the volume- or surface-symmetry energies in nuclei.

The search for an IVQ resonance of the RPA-predicted parameters was motivated by the success of these calculations in describing the properties of the IVM and GDR. The predicted excitation energy of the IVQ is severely constrained by the requirement that the residual interaction used in the RPA calculations reproduce the asymmetry term in the semiempirical mass formula and the excitation energies of the IVM and GDR. Nonetheless, all the deduced cross sections are consistent with zero, and the upper limits for the light elements correspond to 15–30% of the RPA-DWIA method IV estimates. This is in contrast to the measured ratios of approximately 60% for the IVM and GDR. The upper limits do not increase to more than 40%, even when widths of twice the RPA values are assumed. We emphasize that the upper limits are not very sensitive to variations in the IVM cross sections since the latter are, in any case, smaller than the upper limits at the angles where the IVQ peaks. For the heavier elements the results are not as conclusive: In ^{140}Ce the upper limit is small, but so is the measured IVM cross section. In ^{120}Sn the upper limit is high due to the poor statistics of the data at 15°–28°. In ^{208}Pb the expected IVQ cross section is very small and the excitation of a considerable fraction of the sum rule cannot be excluded.

The fact that we did not observe the IVQ in a reaction that gives GDR and IVM signals is of great interest, since the RPA-DWIA calculations use the same nuclear structure input for all three resonances. Another question is whether the small upper limits in ^{140}Ce, ^{90}Zr, ^{60}Ni, and ^{40}Ca contradict other data. Possible evidence for the IVQ has been found in electron scattering in various nuclei ranging from ^{58}Ni to ^{238}U.[9] The IVQ assignments were made to peaks near excitation energies of $130A^{-1/3}$, MeV whose form factors were consistent with those expected for $E2$ transitions. However, the angular range of data did not reach the maximum of the calculated form factor. The deduced sum rule strengths are model dependent and lie within the range 10–90%. Other possible evidence for the IVQ comes from recent measurement of (n,γ) reactions on ^{208}Pb (Ref. 10) and ^{40}Ca (Ref. 11). The fore-aft asymmetry of the gamma yield was interpreted as being due to an interference between dipole and quadrupole radiations, in the expected energy region of the IVQ. However, the deduced strength of the IVQ depends strongly on the model assumed for the dipole strength in the region of the IVQ.

The ^{40}Ca(n,γ) data were consistent with 35% of IVQ sum rule strength, which corresponds to 100% strength in the T component in ^{41}Ca. However, as this result is model dependent it does not contradict our 30% EWSR upper limit for ^{40}Ca. As for the (e,e′) data, there seems to be an inconsistency only with the approximately 50–80% IVQ sum rule reported for ^{140}Ce and ^{60}Ni,[9] as the strength reported in ^{90}Zr is consistent both with 90% and with 10% of the EWSR due to the large uncertainty involved in the analysis.[9] Thus, it seems that more (e,e′) data on medium and light nuclei are needed in order to establish the presumed observation of an IVQ signal in these nuclei.

However, there may be a more general disagreement between the published interpretation of the (e,e′) data and our $(\pi^\pm,\pi^0)$ results. In the former, a broad peak in the energy spectra at approximately $130A^{-1/3}$ MeV was interpreted as the IVQ, and no IVM strength was reported. In the present work there is a clear IVM signal, but none for the IVQ. Several facts suggest a possible explanation for what appears to be a contradiction. (1) The excitation energies reported in (e,e′) and associated with the IVQ are within 1–2 MeV of our estimated IVM values for the inelastic channel. (2) In electron scattering the $E2$ and $E0$ multipolarities cannot be distinguished by the shapes of the form factors only. They can be clearly distinguished in pion charge exchange at energies near the 3,3 resonance by their very different angular distributions. (3) The calculated $E2$ cross section, which corresponds to the full sum rule strength, is 3 times the equivalent $E0$ cross section in (e,e′), whereas the situation is reversed in $(\pi^\pm,\pi^0)$. (4) Our estimates for the IVM width in the inelastic channel are approximately 60–80% larger than the values reported in electron scattering. However, the errors in the widths are large in both experiments.

In view of the above, it is quite possible that a considerable part of the strength which was identified in electron scattering as $E2$ could, in fact, be due to the IVM. For example, the interpretation that 50—80% of the $E2$ sum rule strength is observed in ^{60}Ni(e,e′) is not unique: The (e,e′) data are also consistent with approximately 70% $E0$ and 25% $E2$, as suggested by the (π^-,π^0) results.

VII. CONCLUSIONS

The $(\pi^{\pm},\pi^0)$ reactions were used to study selectively isovector electric resonances. The (π^-,π^0) reaction is especially suitable for studies of the IVM, which was the main motivation for this work. The extensive angular range of the measurements also allowed a reliable search for the IVQ.

A quantitative analysis could be performed only after a considerable effort was made to describe the nonresonant background. The π^- data on the heavy elements, where the IVM and GDR contribute to the cross section only in small regions of energy loss and q^2, were instrumental to our understanding of the background. An examination of the angular variation of the (π^-,π^0) cross sections shows a forward-peaked feature, which follows the $L=0$ angular distribution superimposed on an almost isotropic background. This feature was identified with the IVM. The IVM was more difficult to observe in the (π^+,π^0) reactions. A consistent treatment of the background for all nuclei and angles revealed the IVM in the latter reactions as well. However, the fitting errors, especially for the heavy elements, are generally larger than for the (π^-,π^0) results.

The observation of the IVM in all the $(\pi^{\pm},\pi^0)$ reactions indicates that it is a general feature of nuclei. The IVM and GDR cross sections exhaust the same substantial fraction of the RPA-DWIA estimates, indicating that the IVM is as collective as the GDR. It is well known that the GDR is highly collective and exhausts a large part of the sum rule, which implies that this is equally true for the IVM. The measured energies and widths of the IVM are smooth functions of the nuclear mass and are in good agreement with RPA calculations. Our estimated values for the IVM excitation energies in the inelastic scattering channel follow the function $(59.2\pm2)A^{-1/6}$ MeV. The IVM (π^-,π^0) cross sections decrease with increasing target isospin, due to Pauli blocking for the $T+1$ component. The above properties characterize the IVM as an isovector giant resonance.

The $T+1$ and $T-1$ components of the GDR show up in the 15° energy spectra as clearly identifiable peaks at the expected energies. The fact that the IVM and GDR were analyzed simultaneously, and the fact that the results for the GDR are in good agreement with other data, give a measure of the reliability of the IVM results.

We searched in the π^- data for an IVQ having the properties predicted by RPA-DWIA calculations. The cross sections are consistent with zero in all nuclei. The upper limits for the light elements are well below the fraction of sum-rule strength observed for the IVM and GDR. For the heavy elements the measurements are not sufficiently sensitive to set meaningful limits. The results for the light nuclei seem inconsistent with previous interpretations of electron-scattering experiments that show possible evidence for the IVQ. In view of our results, it is possible that part of the cross section that was attributed in these experiments to the IVQ could, in fact, be due to an IVM excitation. The absence of evidence for an IVQ in the experimental data contradicts the predictions of RPA-DWIA calculations, which predict a compact IVQ.

Pion charge-exchange experiments at energies below and above 165 MeV are in progress to study the effects of different pion interaction radii, and possibly to get better signal-to-background ratios. Other charge-exchange experiments, such as (n,p),[45] (p,n),[46] and $(\bar{p},\bar{n})$,[47] are also planned in order to study the spin-flip modes of the isovector monopole, dipole, and quadrupole excitations. We expect that these experiments will be complementary to the present work in studying isovector resonances.

ACKNOWLEDGMENTS

We wish to thank N. Auerbach, M. B. Johnson, Amir Klein, and E. R. Siciliano for many valuable discussions. This work was supported by the U.S.-Israel Department of Energy and the U.S.-Israel Binational Science Foundation, Jerusalem.

*Present address: Lawrence Berkeley Laboratory, Berkeley, CA 94720.
†Present address: Tel Aviv University, Tel Aviv, Israel.
‡Present address: SIN, Villigen, Switzerland.

[1]A. Bohr and B. R. Mottelson, *Nuclear Structure* (Benjamin, New York, 1975), Vol. II, p. 382.
[2]G. C. Baldwin and G. S. Kleiber, Phys. Rev. **73**, 1156 (1984).
[3]A van der Woude, in *Giant Multipole Resonances,* edited by F. E. Bertrand (Harwood, London, 1979); D. H. Youngblood, *ibid.*
[4]A. Bohr and B. R. Mottelson, *Nuclear Structure,* Ref. 1, Vol. II, p. 670.
[5]N. Auerbach, Nucl. Phys. **A182**, 247 (1972); G. F. Bertsch and S. F. Tsai, Phys. Rev. C **18**, 125 (1975); K. F. Liu and G. E. Brown, Nucl. Phys. **A265**, 384 (1976); A. Z. Mekjian, Phys. Rev. Lett. **25**, 888 (1970).
[6]N. Auerbach and Amir Klein, Phys. Rev. C **28**, 2075 (1983); Amir Klein, Ph.D. thesis, Tel-Aviv University, 1984; N. Auerbach, private communication.
[7]J. D. Bowman, H. W. Baer, R. Bolton, M. D. Cooper, F. H. Cverna, N. S. P. King, M. Leitch, H. S. Matis, A. Erell, J. Alster, A. Doron, M. A. Moinester, E. Blackmore, and E. R. Siciliano, Phys. Rev. Lett. **50**, 1195 (1983); A. Erell, Ph.D. thesis, Tel-Aviv University, 1984 (unpublished); A. Erell, LAMPF Report No. LA-UR-86-1205, 1986 (unpublished).
[8]A. Erell, J. Alster, J. Lichtenstadt, M. A. Moinester, J. D. Bowman, M. D. Cooper, F. Irom, H. S. Matis, E. Piasetzky, U. Sennhauser, and Q. Ingram, Phys. Rev. Lett. **52**, 2134 (1984).

[9]R. P. Pitthan, in *Giant Multipole Resonances,* Ref. 3.
[10]D. M. Drake, S. Joly, L. Nilsson, S. A. Wender, K. Aniol, I. Halpern, and D. Storm, Phys. Rev. Lett. **47**, 1581 (1981).
[11]I. Berqvist, R. Zorro, A. Hakanson, A. Lindholm, L. Nilsson, O. Olsson, and A. Likar, University of Lund Report, 1984 (unpublished).
[12]S. S. Hanna, in *Giant Multipole Resonances,* Ref. 3.
[13]N. Auerbach, Phys. Rev. **98**, 273 (1983).
[14]J. D. Bowman, M. B. Johnson, and J. W. Negele, Phys. Rev. Lett. **46**, 1614 (1981).
[15]Avraham Gal, Phys. Rev. C **25**, 2680 (1982).
[16]V. A. Madsen, F. Osterfeld, and J. Wambach, in *Giant Multipole Resonances,* Ref. 3.
[17]H. W. Baer, R. Bolton, J. D. Bowman, M. D. Cooper, F. H. Cverna, N. S. P. King, M. Leitch, H. S. Matis, A. Erell, J. Alster, A. Doron, M. A. Moinester, E. Blackmore, and E. R. Siciliano, Phys. Rev. Lett. **49**, 1376 (1982).
[18]U. Sennhauser, E. Piasetzky, H. W. Baer, J. D. Bowman, M. D. Cooper, H. S. Matis, H. J. Ziock, J. Alster, A. Erell, M. A. Moinester, and F. Irom, Phys. Rev. Lett. **51**, 1321 (1983).
[19]B. J. Dropesky, G. W. Butler, C. J. Orth, R. A. Williams, M. A. Yates-Williams, G. Friedlander, and S. B. Kauffman, Phys. Rev. C **20**, 1814 (1979).
[20]H. W. Baer, R. D. Bolton, J. D. Bowman, M. D. Cooper, F. H. Cverna, R. H. Heffner, C. M. Hoffman, N. S. P. King, Jose Piffaretti, J. Alster, A. Doron, S. Gilad, M. A. Moinester, P. R. Bevington, and E. Winkelmann, Nucl. Instrum. Methods **180**, 445 (1981).
[21]S. Gilad, Ph.D. thesis, Tel-Aviv University, 1979 (unpublished).
[22]G. Rowe, M. Salomon, and R. H. Landau, Phys. Rev. C **18**, 584 (1978).
[23]V. J. Courtney and J. D. Fox, At. Data Nucl. Data Tables **15**, 141 (1975).
[24]D. Ashery, D. F. Geesaman, R. Holt, H. E. Jackson, J. R. Specht, K. E. Stephenson, R. R. Segel, P. Zupranski, H. W. Baer, J. D. Bowman, M. D. Cooper, M. Leitch, A. Erell, J. Comuzzi, R. P. Redwine, and D. Tieger, Phys. Rev. C **30**, 946 (1984).
[25]Q. Ingram, in *Meson Nuclear Physics—1979,* AIP Conf. Proc. No. 54, edited by E. V. Hungerford III (AIP, New York, 1979).
[26]G. Dakhno and Yu. D. Prokoshkin Yad. Fiz. **7**, 565 (1968). [Sov. J. Nucl. Phys. **7**, 351 (1968)]; H. W. Baer, K. M. Crowe, and P. Truöl, Adv. Nucl. Phys. **9**, 177 (1977).
[27]G. F. Bertsch and O. Scholten, Phys. Rev. C **25**, 804 (1982).
[28]R. Corfu, J. P. Egger, F. Goetz, P. Gretillat, C. Perrin, and R. E. Mischke, in *Meson Nuclear Physics—1979,* Ref. 25; R. A. Eisenstein, *ibid.*
[29]N. Auerbach, M. B. Johnson, Amir Klein, and E. R. Siciliano, Phys. Rev. C **29**, 526 (1984).
[30]S. Adachi and N. Auerbach, Phys. Lett. **131B**, 11 (1983).
[31]W. A. Sterrenburg, Sam M. Austin, R. P. Devito, and Aaron Galonski, Phys. Rev. Lett. **45**, (1980).
[32]*Atlas of Photoneutron Cross Sections,* edited by B. L. Berman (LLNL, Livermore, 1976).
[33]K. Shoda, Phys. Rep. **53**, 341 (1979).
[34]M. Hasinoff, G. A. Fisher, and S. S. Hanna, Nucl. Phys. **A216**, 2221 (1973).
[35]T. J. Bowles, R. J. Holt, H. E. Jackson, R. D. McKeown, A. M. Nathan, and J. R. Specht, Phys. Rev. Lett. **48**, 986 (1982).
[36]J. Ullman, Ph.D. thesis, University of California, Davis, 1981 (unpublished).
[37]B. Schwesinger and J. Wambach, Phys. Lett. **131B**, 29 (1984).
[38]R. Leonardi, Phys. Rev. C **14**, 385 (1976).
[39]N. Auerbach and A. Yeverechyahu, Nucl. Phys. **A332**, 173 (1979).
[40]A. Bohr and B. Mottelson, *Nuclear Structure* (Benjamin, New York, 1969), Vol. 1.
[41]N. Auerbach, Phys. Rev. Lett. **49**, 913 (1982).
[42]H. Uberall, *Electron Scattering from Complex Nuclei* (Academic, New York, 1971), Sec. 6.7.
[43]H. Steinwedel and J. H. Jensen, Z. Naturforsch. **52**, 413 (1950).
[44]M. Goldhaber and E. Teller, Phys. Rev. **74**, 1046 (1948).
[45]N. S. P. King *et al.*, LAMPF Proposal No. 823, 1983 (unpublished).
[46]B. M. Spicer and M. A. Moinester, TRIUMF Proposal No. 271/280, 1983 (unpublished).
[47]A. I. Yavin *et al.*, CERN (LEAR) Proposal, 1985 (unpublished).